J. Fluid Mech. (1998), *vol.* 354, *pp.* 69–100. Printed in the United Kingdom

Dynamics of a vortex ring moving perpendicularly to the axis of a rotating fluid

By A. H. M. EISENGA[1], R. VERZICCO[2] AND G. J. F. VAN HEIJST[1]

[1] Fluid Dynamics Laboratory, Eindhoven University of Technology, PO Box 513, 5600 MB Eindhoven, The Netherlands

[2] Università di Roma "La Sapienza", Dipartimento di Meccanica e Aeronautica, via Eudossiana n^o 18, 00184 Roma, Italy

(Received 8 January 1997 and in revised form 4 June 1997)

The dynamics of a vortex ring moving orthogonally to the rotation vector of a uniformly rotating fluid is analysed by laboratory experiments and numerical simulations. In the rotating system the vortex ring describes a curved trajectory, turning in the opposite sense to the system's anti-clockwise rotation. This behaviour has been explained by using the analogy with the motion of a sphere in a rotating fluid for which Proudman (1916) computed the forces acting on the body surface. Measurements have revealed that the angular velocity of the vortex ring in its curved trajectory is opposite to the background rotation rate, so that the vortex has a fixed orientation in an inertial frame of reference and that the curvature increases proportionally to the rotation rate.

The dynamics of the vorticity of the vortex ring is affected by the background rotation in such a way that the part of the vortex core in clockwise rotation shrinks while the anti-clockwise-rotating core part widens. By this opposite forcing on either side of the vortex core Kelvin waves are excited, travelling along the toroidal axis of the vortex ring, with a net mass flow which is responsible for the accumulation of passive scalars on the anti-clockwise-rotating core part. In addition, the curved motion of the vortex ring modifies its self-induced strain field, resulting in stripping of vorticity filaments at the front of the vortex ring from the anti-clockwise-rotating core part and at the rear from the core part in clockwise rotation. Vortex lines, being deflected by the main vortex ring due to induction of relative vorticity, are stretched by the local straining field and form a horizontally extending vortex pair behind the vortex ring. This vortex pair propagates by its self-induced motion towards the clockwise-rotating side of the vortex ring and thus contributes to the deformation of the ring core. The deflection of vortex lines from the main vortex ring persists during the whole motion and is responsible for the gradual erosion of the coherent toroidal structure of the initial vortex ring.

1. Introduction

Free shear flows subjected to background rotation have been studied extensively because of their relevance to geophysical flows and technical applications. For example, the steady uniform rotation of the Earth implies that atmospheric and ocean eddies are affected by the Coriolis force: depending on their size and mean velocity scales the Rossby number (expressing the relative importance of inertial and Coriolis

forces) of these flow structures can vary from $O(10^{-2})$ to $O(10^{2})$. Background rotation or swirl is also fundamental in turbo-machinery and combustion chambers whose efficiency is severely influenced by the interaction between mean flow and imposed rotation.

Tritton (1992) and Métais *et al.* (1995) (see also several references therein) have studied the effect of background rotation on coherent structures, with the background rotation oriented such that the system vorticity was either parallel or anti-parallel to the local relative vorticity. Verzicco *et al.* (1996) have considered the dynamics of a vortex ring translating in the same direction as the rotation vector, so that the system vorticity was orthogonal to the ring vorticity. In flows of practical interest, however, the angle between the local relative vorticity and the system rotation covers a wide range of orientations. These flows, consisting of many interacting vortex structures, are generally quite complex and their study is very difficult. However, if the investigation is restricted to study only a single vortex structure with an initially symmetric structure, a profound analysis of the flow dynamics is attainable. Therefore, the motion of a single vortex ring is considered, oriented in a direction *orthogonal* to the rotation vector, hence in a horizontal plane. Although this vortex has a 'simple' and well-known structure, all possible orientations between relative vorticity and system rotation are incorporated. A detailed study of this problem can provide substantial insight into the dynamics of complex vortical flows in rotating environments.

In the 1920s, in one of his celebrated papers, Taylor (1921) describes the results of an experiment in which a vortex ring is created in a rotating fluid. The direction of propagation of the vortex ring was perpendicular to the axis of rotation of the fluid. He observed that the vortex ring moved in a curved path relative to the rotating fluid, its path being deflected in the clockwise direction if the fluid was rotating anti-clockwise. He performed this experiment in order to demonstrate the difference between two- and three-dimensional motion in a rotating fluid. He also conducted experiments in which a cylinder and a sphere (with the same density as the fluid) were drawn horizontally through the rotating fluid. As predicted theoretically in previous papers (Proudman 1916; Taylor 1917) the two-dimensional motion generated by the cylinder was not affected by the rotation of the system, and the cylinder moved in a straight line relative to the rotating fluid. For the three-dimensional motion generated by the sphere it was predicted that a net Coriolis force acts perpendicularly to the direction of motion, causing the followed path to deviate from a straight line. In analogy to the sphere, the vortex ring was then expected to move along a circular path relative to the rotating system. In the experiments of Taylor, however, no attention was paid to the evolution of the structure of the vortex ring.

It is well-known that the background rotation of the system serves as a source for the production of relative vorticity. In our previous paper (Verzicco *et al.* 1996) on the motion of a vortex ring along the axis of rotation it was shown that the flow generated by the vortex ring induces relative vorticity that in turn dominates the successive evolution of the flow field. In the case considered in the present paper, again, due to the rotation a secondary flow is induced by the vortex ring. The structure of the secondary flow is in this case completely different, but the generation and evolution of the flow field can still be studied in detail, because of the symmetric geometry of the vortex ring. Using results of both laboratory experiments and numerical simulations it will be shown that the background vorticity influences the evolution of the vortex ring in a surprising way.

The structure of this paper is as follows: in the next two sections the experimental set-up and the numerical code are briefly described. Then, the combined results of laboratory experiments and numerical simulations will be analysed and discussed in order to provide more physical insight into the observed flow phenomena. Special attention is paid to the structure of the flow in the horizontal cross-sectional plane through the vortex ring centre, which serves as a symmetry plane of the flow. A complete picture of the evolution of the three-dimensional structure of the vortex is obtained from numerical simulations solely. Closing remarks are given in § 5. An Appendix is added at the end in which the main results of some classical papers (Proudman 1916; Taylor 1917, 1923) are briefly summarized, since these are necessary for the discussion of the curved ring trajectory.

2. Experimental set-up

The vortex ring generator used in the present laboratory experiments has already been used in the experiments in a previous work and it is described in detail in Verzicco *et al.* (1996). Only the adjustments to the experimental set-up that were necessary to perform the experiments described in this paper are mentioned here.

The vortex ring generator, consisting of a closed cylindrical box with a sharp-edged circular orifice on top, could be rotated around a horizontal axis in a fork that was fixed to a stand. In the study in Verzicco *et al.* (1996) the generator was oriented such that vortex rings were fired vertically upwards. In the experiments presented here the generator was rotated 90° and the vortex rings created propagated in a horizontal direction. The vortex ring generator was positioned near the centre of a large experimental tank of horizontal dimensions 150×100 cm and 30 cm height (see figure 1). The tank was placed on a rotating table, whose angular velocity could be varied between $\Omega = 0.06\ \mathrm{s}^{-1}$ and $\Omega = 0.2\ \mathrm{s}^{-1}$. The centreline of the orifice in the generator was directed towards the centre of the rotating table.

A horizontal light sheet was used to illuminate the cross-section of the vortex ring in a plane through the centre of the orifice. This light sheet was created by a slide projector provided with a black slide with a narrow slit. Two adjacent slide projectors, put on one side of the tank on a platform fixed to the rotating table, created a thin horizontal light sheet spanning a large horizontal area. All experiments were recorded from above by a video camera mounted on a frame attached to the rotating table.

Fluorescein dye was used to visualize the flow field. The fluid in the vortex ring generator was slightly dyed and the tank was filled with clear tap water to a level of 20 cm, the distance from the orifice centre to the free surface level and the bottom of the tank being 10 cm. To avoid mixing during filling of the tank, the orifice was temporarily closed by a metal plate. Before the experiments were started the water in the tank had to spin-up for about one hour in order to achieve a state of uniform rotation and then the metal plate could be pushed aside carefully.

A vortex ring was created by pushing a finite amount of fluid through the orifice, at the sharp edge of which a vortex sheet rolled up into a vortex ring. The injection of fluid was controlled by a stepmotor-driven traversing system, pushing a set-up of six syringes simultaneously. From previous studies (see Verzicco *et al.* 1996) it is known that, for an orifice with diameter $D_o = 4$ cm, a fluid injection with slug length $L_o = 2.4$ cm and mean injection velocity $U_o = 2.4\ \mathrm{cm\,s}^{-1}$ at the generator orifice produces a steady laminar vortex ring in a fluid at rest. The same fluid injection parameters were used in the present experiments.

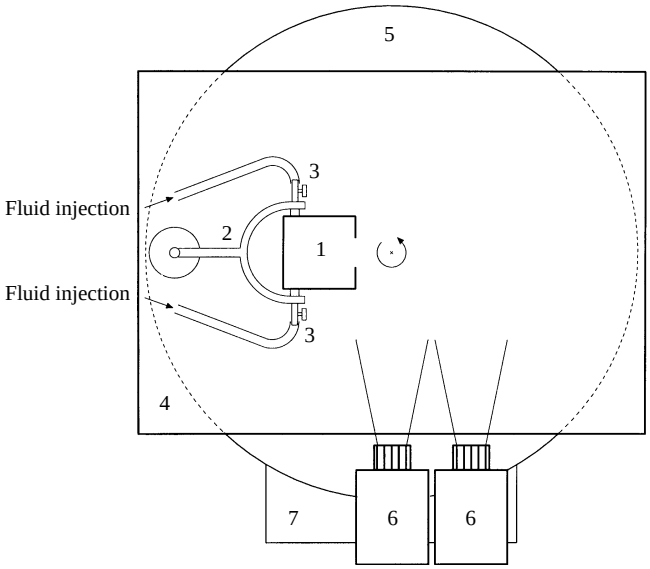

FIGURE 1. Schematic top view of the experimental set-up. Vortex ring generator **1** is turned in the fork **2** so that vortex rings are fired in horizontal direction. Tubes for fluid injection are connected to the generator by two watertaps **3**. The set-up is placed in a tank **4**, filled with water, on top of a rotating table **5**. The sense of rotation of the table is denoted by an arrow. Two slide projectors **6**, put on one side of the tank on a platform **7** fixed to the table, are used to produce a wide light sheet to illuminate the flow in a plane through the vortex ring centre. A video camera (not shown) mounted above the table records a top view of the experiment relative to the rotating system.

3. Numerical set-up

3.1. *Equations of motion and numerical scheme*

The flow in a rotating fluid is commonly described relative to axes rotating steadily with the fluid. In a frame rotating with angular velocity $\boldsymbol{\Omega} = \Omega \boldsymbol{k}$ (with $\boldsymbol{k}$ the unit vector directed along the axis of rotation) the relative velocity $\boldsymbol{u}$ of an incompressible viscous fluid satisfies the Navier–Stokes and continuity equations, written as

$$\left.\begin{aligned} \frac{\mathrm{D}\boldsymbol{u}}{\mathrm{D}t} \equiv \frac{\partial \boldsymbol{u}}{\partial t} + (\boldsymbol{u}\cdot\nabla)\boldsymbol{u} = -\nabla p - \frac{1}{Ro}\boldsymbol{k}\times\boldsymbol{u} + \frac{1}{Re}\nabla^2\boldsymbol{u}, \\ \nabla\cdot\boldsymbol{u} = 0, \end{aligned}\right\} \tag{3.1}$$

with $\mathrm{D}/\mathrm{D}t \equiv \partial/\partial t + \boldsymbol{u}\cdot\nabla$ the material derivative operator. The pressure p is the reduced pressure, which includes the potential of the centrifugal force. These equations have been written in dimensionless terms using the toroidal radius $\mathscr{L}$ and circulation Γ of the initial vortex ring. In terms of these scales the Rossby number is defined as $Ro = \Gamma/2\Omega\mathscr{L}^2$ and the Reynolds number as $Re = \Gamma/\nu$, with ν the kinematic viscosity of the fluid.

In flow visualization experiments passive tracers (e.g. fluorescein dye) are used to infer typical features in the flow development and to track the position of the vortex structure in time. In order to obtain a closer comparison between the results of these flow visualization experiments and numerical simulations, the evolution of the concentration C of such a passively advected tracer is simulated, according to the equation

$$\frac{\mathrm{D}C}{\mathrm{D}t} = \frac{1}{ReSc}\nabla^2 C. \tag{3.2}$$

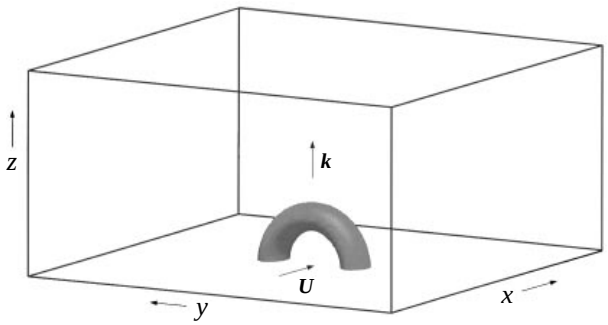

FIGURE 2. Perspective view of the computational box and the initial configuration of the vortex ring, with propagation direction $\boldsymbol{U}$ oriented orthogonal to the unit vector $\boldsymbol{k}$ of the rotation. The boundary conditions at the bottom surface imply the presence of an image vortex below the computational box that completes the vortex ring.

The Schmidt number Sc is defined as the ratio between the kinematic viscosity ν of the fluid and the diffusivity κ of the tracer.

Equations (3.1) and (3.2) have been written in a Cartesian coordinate system and discretized by centred finite-difference schemes, second-order accurate in space and in time. In the limit $\nu \to 0$ the energy is conserved by (3.1) and the numerical scheme is such that this holds in the discretized equations. The discretization is uniform in all spatial directions. The numerical method is similar to that described by Orlandi (1990) which has the following features. The discretized equations are solved by a fractional-step method (Kim & Moin 1985) with the viscous terms computed implicitly and the convective terms explicitly. The large sparse matrix resulting from the implicit terms is inverted by an approximate factorization technique. At each time step the momentum equations are provisionally advanced using the pressure at the previous time step, giving an intermediate non-solenoidal velocity field. A scalar quantity Φ is then introduced to project the non-solenoidal field onto a solenoidal one. The large band matrix associated with the elliptic equation for Φ is reduced to a tridiagonal matrix using trigonometric expansions in the periodic directions. The pressure at the new time is also computed from the scalar Φ. The advancement in time of the equations is obtained by a hybrid third-order Runge–Kutta scheme which, owing to its large stability limit ($CFL \leqslant \sqrt{3}$), allows CPU-time savings.

3.2. *Initial configuration and convergence checks*

The initial flow configuration is shown in figure 2 and consists of a vortex ring located at the centre of a computational box. The axial centreline of the vortex ring is oriented parallel to the x-axis and the unit vector $\boldsymbol{k}$, denoting the rotation axis, is directed along the z-axis of a Cartesian coordinate system, the vortex ring propagating with velocity vector $\boldsymbol{U}$. Laboratory experiments have shown that, even if the rotation is present, the flow field remains symmetric relative to a horizontal plane through the centreline of the vortex ring. To save computational effort it is therefore sufficient to simulate only one half of the vortex ring, the symmetry plane $z = 0$ being the bottom surface of the computational domain. The proper boundary conditions at this side, i.e. vanishing normal velocity component and zero shear stresses, then imply the presence of an image vortex that completes the vortex ring. These boundary conditions are also imposed at the top surface, while periodicity is assumed at the lateral surfaces.

The domain is chosen sufficiently large to exclude artificial perturbations of the

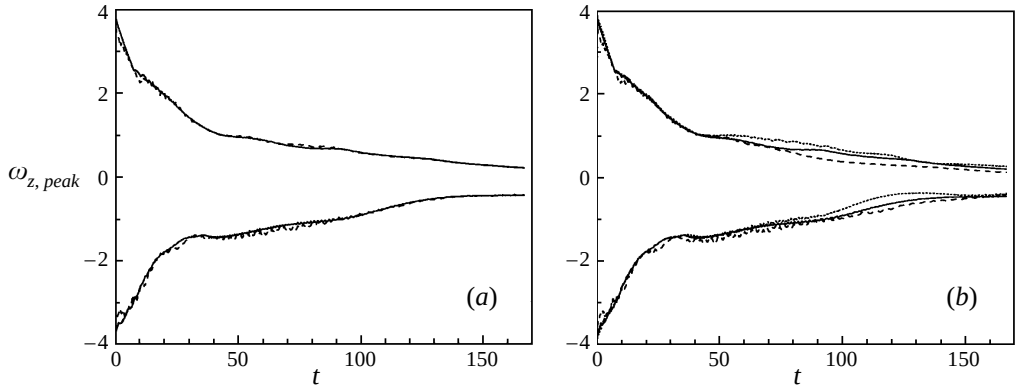

FIGURE 3. Time evolution of the positive and negative peak vorticities ω_z in the horizontal symmetry plane $z = 0$ of the flow, obtained from numerical simulations with $Ro = 23$ and $Re = 900$. (*a*) Grid refinement check with fixed box size 8×8×4: fine grid 97×97×49 (solid lines) and coarse grid 65×65×33 (dashed lines). (*b*) Domain dimensions check: small box 6×6×3 (dotted lines, grid 65×65×33), intermediate box 8×8×4 (solid lines, grid 97×97×49) and large box 12×12×6 (dashed lines, grid 97×97×49).

flow introduced by the periodicity and finiteness of the domain. This is checked by simulations with different box sizes. Furthermore, the number of grid points employed has been submitted to a grid refinement check. For these checks the evolution of the peak values of the vorticity of the flow are examined: the positive and negative peaks of the axial vorticity component ω_z in the plane $z = 0$ can be shown to be representative of the vorticity maxima of the flow. Figure 3(*a*) shows the time evolution of the positive and negative peak values of ω_z for two simulations with a fine grid 97×97×49 and a coarse grid 65×65×33, respectively, in a box with fixed dimensions 8×8×4 in the *x*-, *y*- and *z*-directions. This check confirms that the finer grid is sufficient to describe the vortex ring evolution. Figure 3(*b*) shows the results of simulations with three different box sizes and the profiles of ω_z display only a minor dependence on the dimensions of the box. In conclusion, a box with intermediate dimensions 8×8×4 with a fine grid 97×97×49 has been employed for the simulations presented in this paper. A refinement check was also performed for the time step size and it was mostly taken $\Delta t = 0.1$, according to a *CFL* number $< \sqrt{3}$ as imposed by the stability limit of the time integration scheme†.

In this numerical code the initial structure of the vortex ring has to be assigned explicitly. In the previous paper (Verzicco *et al.* 1996) a different numerical code written in cylindrical coordinates was used in which the generation and evolution of a vortex ring as produced experimentally by the ejection of a finite amount of fluid from a circular orifice was simulated. In that paper the initial parameters for the numerical simulations were adjusted so that they mimic the laboratory experiments very well. Taking advantage of the fact that both the experimental set-up and the ring parameters were the same as in the present study, the initial vortex ring obtained in that previous study will be used as initial configuration for the present simulations. More precisely, the vortex structure used has already been formed in a simulation without background rotation performed with the code in cylindrical coordinates. The

† The maximum velocity of the flow determines in combination with the grid spacing and the time step Δt the *CFL* number of the flow. For the present simulation the maximum velocity is $|\boldsymbol{u}|_{max} \simeq 0.7$ at $t = 0$, yielding $CFL \sim (|\boldsymbol{u}|_{max}\Delta t/\Delta x) = 0.84$.

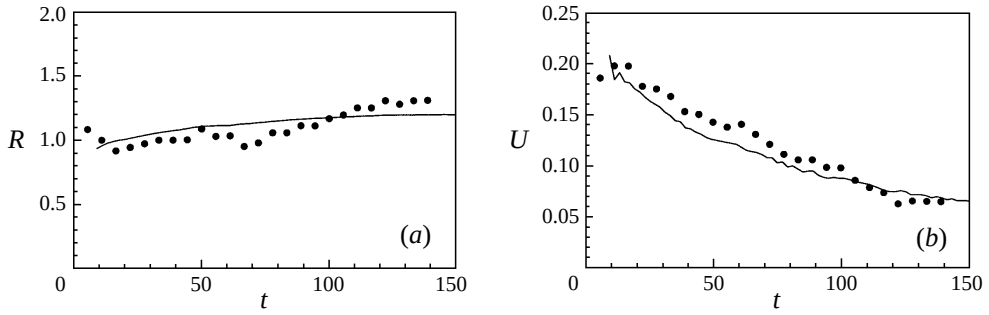

FIGURE 4. Evolution of (a) the ring radius R and (b) the velocity of propagation U of a vortex ring without background rotation ($Re = 900$). Experimental data are denoted by symbols and results of the numerical simulation by solid lines. Experimental parameters: $D_o = 4.0$ cm, $L_o = 2.4$ cm and $U_o = 2.4\ \mathrm{cm\,s^{-1}}$. The numerical simulation is started with a vortex ring that has been formed in a preliminary simulation with a different numerical code in a time $t' = 4$. According to the present time scaling, this corresponds to a time $t = 9.2$ during which the vortex ring already has evolved before the actual simulation is started. In the figure the data from the simulation are therefore plotted from $t = 9.2$.

initial three-dimensional fields necessary to start the numerical simulations with the present code in Cartesian coordinates are then obtained by standard interpolation procedures from the axisymmetric flow field of this initial vortex structure.

3.3. *Scaling of the experiment*

The scaling of the experiment to the numerical simulation was checked by experiments without background rotation, performed with the present experimental set-up. In these experiments the injection parameters $L_o = 2.4$ cm and $U_o = 2.4\ \mathrm{cm\,s^{-1}}$ were used that lead to the formation of a steadily propagating laminar vortex ring from a 4 cm orifice. Video images of dye experiments taken at successive time steps were used to measure the evolution of the ring radius R and the propagation velocity U in time. The same ring parameters are obtained from a numerical simulation without background rotation, started with the vortex ring described in the previous section. The results of both the experiment and the simulation are shown in figure 4. In this graph the experimental values of the ring radius and the velocity of propagation have been scaled by a length scale $\mathscr{L} = 1.8$ cm (denoting, approximately, the dimensional value of the initial ring radius) and velocity scale $\mathscr{V} = 5.0\ \mathrm{cm\,s^{-1}}$, respectively. Using this velocity scale the initial value of the vortex ring propagation velocity, being $1\ \mathrm{cm\,s^{-1}}$ in the experiment, matches approximately the initial value for U in the simulation. From $\mathscr{V} = \Gamma/\mathscr{L}$ it follows that $\Gamma = 9.0\ \mathrm{cm^2\,s^{-1}}$. Accordingly, the time axis is scaled by $\mathscr{T} = \mathscr{L}^2/\Gamma = 0.36$ s. These scales are then used to determine the Reynolds number $Re = \Gamma/\nu = 900$ and the Rossby number $Ro(\Omega) = \Gamma/2\Omega\mathscr{L}^2 = 1.4/\Omega$, which are specific parameters for the numerical simulations. Among all parameters only the rotation rate Ω was varied in the laboratory experiments.

While for Re and Ro it was possible to obtain a proper correspondence between simulation and experiments, the same cannot be done for the Schmidt number. In fact, the small diffusivity of tracers in liquids yields $Sc \approx O(500\text{–}1000)$ which, due to resolution problems, is too large for three-dimensional numerical simulations. Throughout this study a value $Sc = 4$ has been used which, though considerably lower than the experimental value, still describes the effects of the different diffusivities of vorticity and passive scalar. This is important when deducing aspects of vorticity

dynamics from flow visualizations, since small flow scales observed from the tracer might not exist in terms of vorticity.

It should be stressed that a good agreement between experiments and numerical simulations in the absence of background rotation does not imply the same agreement when rotation is present. In the latter case, the flow field is affected at all times by the system rotation, including during the injection of fluid and the formation of the vortex ring. This might lead to an initial configuration different from that of the numerical simulations, where the rotation is imposed over an already existing vortex ring formed in the absence of rotation. In the laboratory experiments only relatively low rotation rates have been used for which it was observed that in the initial stage a vortex ring was formed. As discussed in Verzicco & Orlandi (1996), to understand the physics of the vortex ring evolution the initial vorticity distribution in the vortex core is not particularly important; it is only to have one-to-one correspondence between numerical simulations and laboratory experiments that the same initial vorticity distribution should be used. In the present paper, comparisons between vortex trajectories and vorticity dynamics of the ring core will be presented showing that the differences in the initial structures are of minor importance for the subsequent flow evolution. This implies that the initial conditions mentioned above can be used also in the rotating cases.

4. Results

In order to get a qualitative picture of the flow field, images of a flow visualization experiment are presented first. Using the arguments of Proudman (1916) and a simple inviscid model for the motion of a sphere in a rotating fluid, the curved trajectory of the vortex ring in the rotating system can be explained. Flow visualizations are also used as guidelines for the subsequent analysis of the flow by direct numerical simulations, which give a complete three-dimensional view of the structure. Advantage is taken of the symmetry of the flow and important insight into the flow dynamics is gained by analysing the evolution of the flow in the horizontal plane of symmetry.

4.1. *Flow visualizations*

The sequence of video images presented in figure 5 shows the propagation and evolution of the vortex ring. Only a central cross-section of the vortex ring in a horizontal plane normal to the axis of rotation was illuminated by the light sheet. The images were recorded with a video camera fixed on the rotating table, showing the flow field relative to the rotating frame. The table was rotating in the anti-clockwise direction with a relatively low angular velocity $\Omega = 0.06$ s^{-1}, yielding a Rossby number $Ro = 23$.

From the first image (figure 5*a*) it is seen that after injection of the fluid an axisymmetric vortex ring is created. In case of no rotation of the system this vortex ring would propagate along a straight path. However, from the succeeding images of figure 5 it is clearly seen that in the present case the path of the vortex ring is curved, the ring being deflected in a clockwise direction. Although the vortex ring remains a coherent structure, its shape changes in time and in the cross-sectional views (figure 5*b–f*) a gradual change in the size of the dyed cores is observed. In particular, the part of the core on the inner side of the curved path (henceforth denoted as the 'inner core part') shrinks, while the part of the core on the outer side (the 'outer core part') expands in time. In oblique views of the flow structure (not shown here) it has

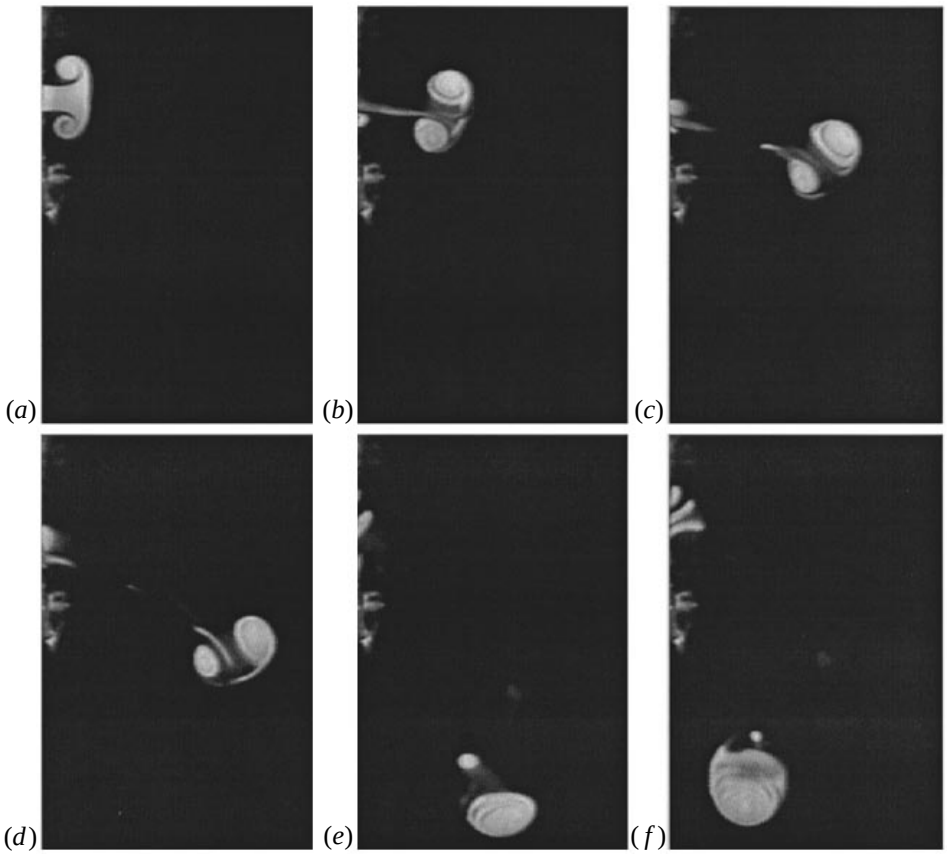

FIGURE 5. Cross-sectional (top) view of the evolution of a vortex ring propagating in a plane perpendicular to the rotation axis along a curved path in clockwise direction, i.e. opposite to the sense of rotation of the system ($Ro = 23$ and $Re = 900$): (*a*) $t = 6$, (*b*) $t = 17$, (*c*) $t = 33$, (*d*) $t = 50$, (*e*) $t = 117$ and (*f*) $t = 150$ after start of the fluid injection. Experimental parameters: $D_o = 4.0$ cm, $L_o = 2.4$ cm, $U_o = 2.4$ cm s^{-1} and $\Omega = 0.06$ s^{-1}.

been observed that the vortex structure as a whole remains approximately circular during most of the motion.

It should be noted that a small filament of dye crosses the front of the vortex ring from the outer core part to the inner core part, as can be observed in figure 5(*d*). In the same figure a second filament of dye is seen to be shed between the two vortex core parts. This filament is different from the trail behind the vortex ring in figures 5(*a*) and 5(*b*), which is just fluid not entrained in the vortex ring during the ring's formation. The creation of both filaments in figure 5(*d*) will be discussed in more detail in §§ 4.3 and 4.4, where the results of numerical simulations are examined.

At a later stage in the evolution the vortex ring is slightly twisted (figure 5*e*) and a horizontal cross-flow of dye from the outer to the inner core part occurs (figure 5*f*). This cross-flow is limited to a narrow band of only a few millimetres thick, located just in the light sheet as observed in an oblique view. After some time, a blob of dyed fluid with hardly any motion remains.

Similar features of the ring dynamics have been observed if the Rossby number is decreased, experiments have been performed to $Ro \simeq 8$. Proportionally to the rotation rate the curvature of the ring trajectory and the respective squeezing and widening

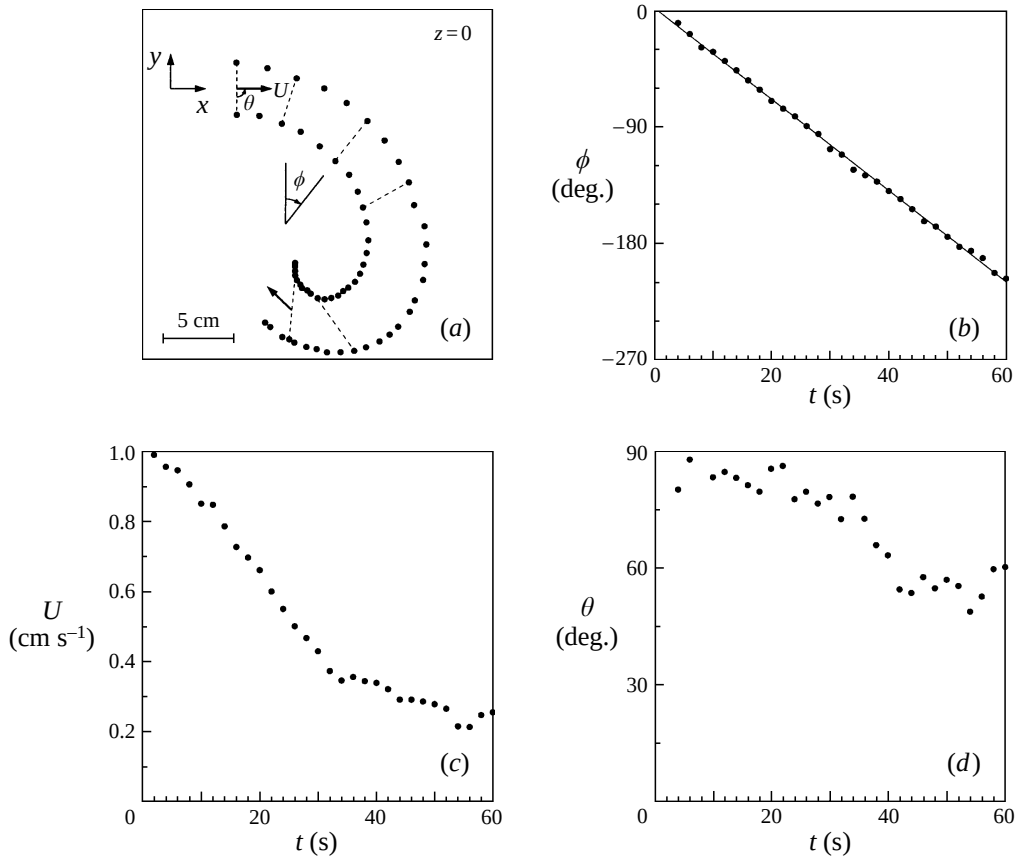

FIGURE 6. (*a*) Trajectory of a vortex ring measured from a dye-visualization experiment with $Ro = 23$ and $Re = 900$. Symbols denote the positions of the core centres at fixed time intervals $\Delta t = 2$ s (first positions measured 2 s after start of fluid injection); the plane of the vortex ring denoted by dashed lines has been drawn at the same instantaneous ring positions as the images shown in figure 5; the initial and final direction of the ring motion are indicated by arrows. (*b*) Rotation ϕ of the plane of the vortex ring in time. (*c*) Decay of vortex ring propagation velocity U. (*d*) Variation in time of angle θ between the plane of the vortex ring and its direction of motion.

of the core sections are enhanced. The curved trajectory of the vortex ring will be discussed in the next subsection and the gradual change of the core cross-sections in § 4.3.

4.2. *Curved trajectory of the vortex ring*

To determine the trajectory of the vortex ring the positions of the centres of the visualized core parts have been measured from video images at successive times and these data are plotted in figure 6 (*a*). At a few positions in its trajectory, marking the instantaneous positions of the vortex ring in the images in figure 5, the plane of the vortex ring is denoted by dashed lines connecting the corresponding core centres; the initial and final direction of propagation of the vortex ring is indicated by arrows. The first part of the curved path is approximately circular and the plane of the vortex ring remains perpendicular to its direction of propagation. At later times, however, this motion is not maintained: the curvature of the path increases and the outer core part seems to lag behind. This situation was apparent in figure 5 (*e*), where the vortex

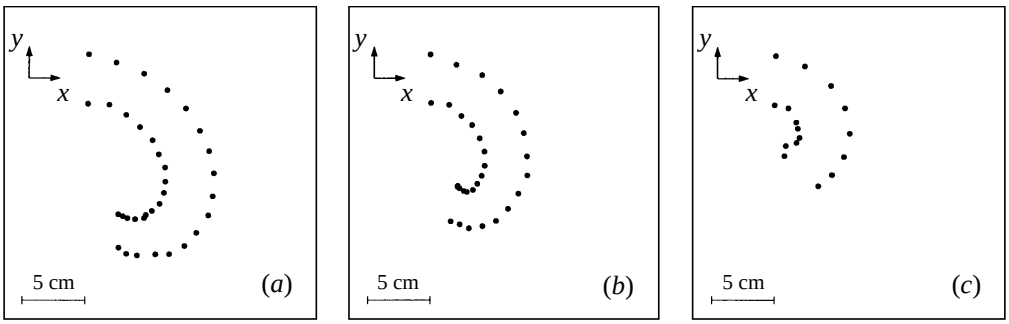

FIGURE 7. Ring trajectories measured from laboratory experiments with $Re = 900$ and different rotation rates: (*a*) $Ro = 16$ ($\Omega = 0.09\ \mathrm{s}^{-1}$), (*b*) $Ro = 13$ ($\Omega = 0.11\ \mathrm{s}^{-1}$) and (*c*) $Ro = 8.2$ ($\Omega = 0.17\ \mathrm{s}^{-1}$). In all cases symbols are plotted at $\Delta t = 2$ s (cf. figure 6*a*).

ring was seen to be twisted. Clearly, the direction of propagation of the vortex ring at this stage is no longer perpendicular to the plane of the vortex ring.

The angle ϕ over which the plane of the vortex ring rotates has been measured as a function of time and the results are plotted in figure 6(*b*). The orientation angle decreases steadily, implying that the vortex ring rotates with a constant angular velocity (in a clockwise direction), whose value is obtained from the slope of these data points. Using a linear regression, given by the straight line in figure 6(*b*), a value $\Omega_{v.r.} = -0.06 \pm 0.002\ \mathrm{s}^{-1}$ is obtained, which is exactly opposite to the angular velocity $\Omega = 0.06\ \mathrm{s}^{-1}$ of the rotating table in this experiment. This means that relative to the inertial frame of the laboratory the vortex ring maintains a fixed orientation in space.

Figure 6(*c*) shows the gradual decay of the propagation velocity of the vortex ring. This velocity is calculated from the distance travelled by the midpoint between the core centres in fixed time intervals. Figure 6(*c*) shows a kink in the velocity decay at around $t = 32$ s. At around the same moment there is a strong decrease of the inclination angle θ between the plane of the vortex ring and its direction of propagation (see figure 6*d*). It has been observed from dye-visualization experiments that near the end of the motion the vortex ring is slightly twisted (see figure 5*e*). From figure 6(*d*) it is seen that this twisting of the vortex ring starts at around $t = 32$ s. After this the vortex ring continues its propagation very slowly, but the twisting and deformations of the structure will inevitably lead to its total destruction.

A series of experiments have been performed in which different rotation rates Ω were used with the injection parameters for the vortex ring kept fixed. If the table rotates faster the evolution of the flow field has the same features as described above, although the curvature of the trajectory is enhanced (see figure 7). Experiments were carried out for four different values of the rotation rate, ranging from $\Omega = 0.06\ \mathrm{s}^{-1}$ to $\Omega = 0.17\ \mathrm{s}^{-1}$ ($Ro = 23$ and $Ro = 8.2$, respectively) and the angular velocity $\Omega_{v.r.}$ of the rotating vortex ring was measured in each experiment. The results are summarized in table 1, showing that for all experiments the angular velocity of the rotation of the vortex ring is just equal but opposite to the angular speed of the rotating table, indicating that the vortex ring maintains a fixed orientation relative to the inertial frame of the laboratory.

This property of the horizontal motion of a vortex ring in a rotating fluid had already been observed by Taylor in a similar experiment (Taylor 1917, 1921). However, Taylor did not report measurements on the curved trajectory nor observations about

Exp.	Ω (s^{-1})	$\Omega_{v.r.}$ (s^{-1})
1	0.06	–0.06
2	0.09	–0.101
3	0.11	–0.12
4	0.17	–0.17

TABLE 1. Rotation rate $\Omega_{v.r.}$ of vortex ring in curved motion for four experiments with different angular velocity Ω of the rotating table (measurement inaccuracy $\Delta\Omega_{v.r.} = \pm 0.002$)

the deformation of the vortex structure. He performed this experiment merely to demonstrate the analogy with the horizontal motion of a solid sphere in a rotating fluid. According to theoretical predictions, it was expected that the motion of three-dimensional objects in a rotating fluid is affected by the background rotation. For the experiments with the sphere Taylor built an experimental set-up in which a solid sphere could be towed in a horizontal plane through a rotating fluid by pulling a wire steadily. A homogeneous sphere was used with the same density as the fluid. The path of the sphere was observed to be deflected to the right relative to a system rotating in an anti-clockwise direction.

According to the arguments given by Proudman (1916) (for completeness summarized in the Appendix of this paper) this behaviour can be explained by analysing the balance of the forces acting on the sphere. Consider a homogeneous sphere of mass M with the same uniform density as the fluid. The fluid rotates in an anti-clockwise direction with angular velocity Ω. The sphere propagates relative to the rotating system with velocity U in a direction perpendicular to the rotation axis. The balance of all the forces acting on the sphere (Proudman 1916) gives a net force $\frac{3}{2}M\Omega U$ orthogonal to the trajectory of the sphere to the right, deviating the motion of the sphere in a clockwise direction.

To determine the acceleration of a sphere in response to an applied force a virtual mass $\frac{1}{2}M$, due to the displacement of the surrounding fluid, has to be added to its real mass M, yielding a total mass $\frac{3}{2}M$ (see Batchelor 1967, p. 453, where this is derived for a sphere moving in a fluid otherwise at rest). Supposing that this also holds for the motion of a sphere in a rotating fluid, the acceleration of the sphere due to the force $\frac{3}{2}M\Omega U$ is then given by $a_\perp = \Omega U$, in the same direction as the force. This centripetal acceleration causes the sphere to move along a circular path with radius R_c, according to $a_c = U^2/R_c$. Equating the expressions for $a_\perp$ and a_c then yields the relation:

$$U = \Omega R_c, \tag{4.1}$$

implying that the angular velocity (U/R_c) of the circular motion of the sphere is just equal to the angular velocity of the rotating table, although the sense of the rotation is opposite.

It should be stressed that this model is derived for the motion of a solid sphere in an ideal rotating fluid, which is quite different from the translating vortex ring in the present experiments. In fact, in the derivation of the model (see the Appendix) the pressure force exerted by the surrounding flow on the surface of the sphere (caused by the combined Coriolis forces acting on the fluid elements displaced by the moving sphere) played a crucial role and Proudman (1916) has shown that this force depends on the shape of the solid considered. For example, for a prolate ellipsoid with polar

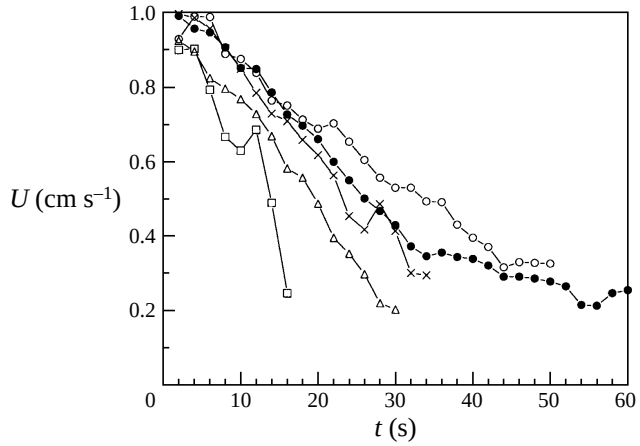

FIGURE 8. Decay of propagation velocity of a vortex ring as measured from dye-visualization experiments with $Re = 900$ and different rotation rates: $Ro = \infty$ (no background rotation) (open circles), $Ro = 23$ (filled circles), $Ro = 16$ (crosses), $Ro = 13$ (triangles) and $Ro = 8.2$ (squares).

axis parallel to the rotation of the system this pressure force is larger than for a sphere, while for an oblate ellipsoid oriented in the same way it is smaller. A vortex ring transports during its motion a closed blob of fluid, called the vortex 'atmosphere' (Thomson 1867). The boundary of this vortex ring atmosphere does not have the shape of a simple mathematical object, and the pressure force cannot be computed analytically. On the other hand, similarly to a sphere (and in contrast to a prolate or an oblate ellipsoid) the vortex ring atmosphere has equal dimensions in the vertical and lateral directions orthogonal to the horizontal propagation. Furthermore, the shape of the boundary of the vortex ring atmosphere in the experiments without background rotation might reasonably be approximated by a spherical surface. Therefore, the mean pressure force at a right angle to the motion of the vortex ring is assumed to be equal to the force exerted on a sphere. The motion of the vortex ring is then given by (4.1), which describes a curved path with angular velocity equal but opposite to the rotation rate of the table. Unlike the solid structure of the sphere, the shape of the vortex ring atmosphere is subject to deformations resulting from local variations in the pressure force exerted by the surrounding fluid. Deformations of the vortex ring structure affect the evolution of the flow and will be examined in more detail in § 4.3.

According to (4.1) the ring trajectory is circular only if the propagation velocity U is constant. A decaying velocity results in a decreasing value for the radius of curvature R_c, as displayed by the spiral-shaped trajectory in figure 6 (a). The decay of the velocity U results mainly from viscous diffusion of vorticity, but is enhanced by effects of the rotation through the deformation of the vortex structure. Figure 8 shows the decrease of the propagation velocity of the vortex ring in experiments with different rotation rates of the fluid. The case without background rotation ($Ro = \infty$) is also included, for which the velocity decay is solely due to viscous effects. It is seen that with increasing background rotation (decreasing Ro-values) the velocity decay is enhanced and a substantial retardation of the ring speed is imposed by the system rotation. This phenomenon is related to the vorticity dynamics of the vortex structure in the rotating fluid, which will be examined in the next subsection.

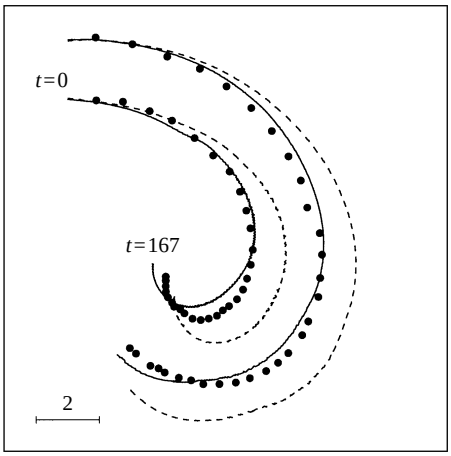

FIGURE 9. Ring trajectories measured from the positions of the core centres in the horizontal symmetry plane $z = 0$ ($Ro = 23$ and $Re = 900$). Experimental data are denoted by symbols (plotted at $\Delta t = 5.6$) and the results from two numerical simulations are plotted by lines. The solid lines denote the ring trajectory from a simulation initiated with a steady vortex ring computed in a preliminary simulation from a finite flow injection. The dashed lines denote the ring trajectory from a simulation initiated with a vortex ring with a Gaussian vorticity profile in the ring core. For experimental parameters: see the caption to figure 5.

4.3. *Vorticity dynamics in the horizontal plane of symmetry*

In the previous subsection the trajectory of the vortex ring was considered and its curvature was explained ignoring the vorticity dynamics. From figure 5, however, it is clear that during the evolution significant changes in the vortex structure occur and these are expected to be related to the effects of the background rotation. A detailed study of the vorticity dynamics from laboratory experiments is hardly possible because of the three-dimensional nature of the flow. In contrast, the complete three-dimensional structure of the evolving vortex ring can be examined by direct numerical simulations, as well as the flow in any cross-sectional plane. Some aspects of the vorticity dynamics conjectured from dye-visualization experiments have been verified by these numerical simulations and, in addition, a detailed analysis of the three-dimensional vortex structure has been performed.

To check the results of the numerical simulations and the scaling of the experiments, the trajectory of the computed vortex ring has been compared with the ring trajectory obtained from a laboratory experiment with the same parameters. The rotation rate of the system in this laboratory experiment was $\Omega = 0.06\ \mathrm{s}^{-1}$, yielding the values $Ro = 1.4/\Omega = 23$ and $Re = 900$ to be used in the simulations (according to the scaling of the experiment). In numerical simulations the ring trajectories are obtained from the successive positions of the vorticity peaks in the horizontal plane $z = 0$ through the centre of the vortex ring. In figure 9 the ring trajectories obtained from the laboratory experiment and corresponding numerical simulation are plotted simultaneously. They show a very nice agreement, taking into account the experimental inaccuracy in the measurement of the positions of the vortex centres from the dyed core patches (see figure 5) and the differences between vorticity and passive scalars mentioned in § 3.3. A better correspondence cannot be expected in view of the different initial conditions used in the numerical simulation. On the other hand, the main features of the flow are insensitive to the initial vorticity distribution in the ring core. To demonstrate this an additional numerical simulation has been carried out which is initiated by a

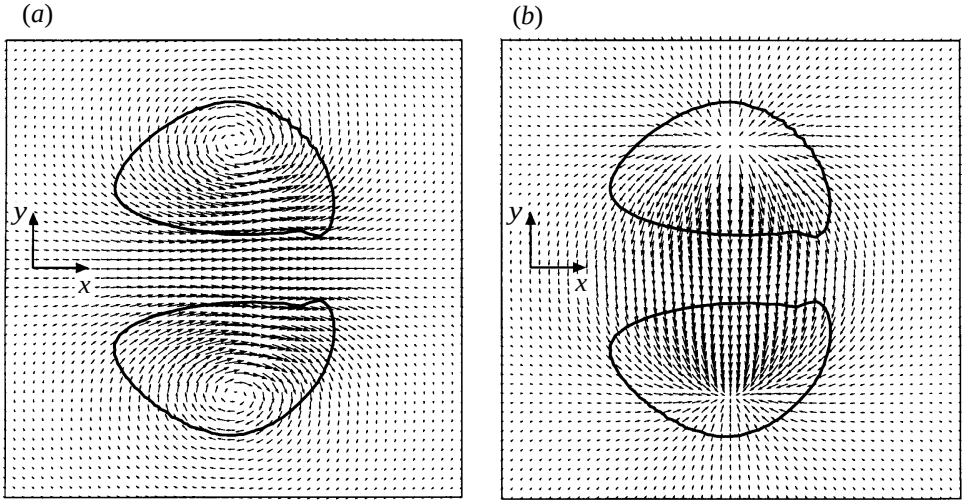

FIGURE 10. (*a*) Velocity vector plot showing the planar flow $\boldsymbol{u_2}$ in the horizontal plane of symmetry $z = 0$ of a vortex ring propagating from left to right. Relative to a system in anti-clockwise rotation, with rotation vector pointing along the z-axis, this flow experiences a Coriolis force proportional to $\boldsymbol{u_2} \times 2\boldsymbol{\Omega}$. The vector field of this force is plotted in (*b*). The thick solid lines are vorticity contours at $|\omega_z| = 0.1$, which are indicative of the boundaries of the cross-sections of the vortex core.

vortex ring with a Gaussian vorticity profile in the ring core. The computed trajectory of this vortex ring is also shown in figure 9, showing a similar curved ring motion; however, the ring trajectory does not match properly with the experimental data in this case. In conclusion, the numerical simulation initiated with a steady vortex ring, being computed in a preliminary simulation from a finite flow injection, mimic the laboratory experiment quite well in the presence of the background rotation; this simulation will now be used to examine the effects of the rotation of the system on the vorticity dynamics of the vortex ring.

As a first step in the analysis of the flow dynamics consider the flow in the horizontal cross-sectional plane through the vortex ring centre. This plane is a mirror plane of the motion, since deformations of the vortex ring due to Coriolis forces appear symmetrically in the upper and lower ring halves, and this feature has already allowed the simulation of only one half of the vortex ring. As a consequence, the flow in this plane is planar and therefore attractive for a detailed analysis. In addition, the computed structure of the flow in this plane can be compared with the video images from the dye-visualization experiment, in which the flow in the same cross-sectional view was recorded. Relative to the Cartesian coordinates defined in figure 2 this planar flow is given by a two-dimensional velocity vector $\boldsymbol{u_2}$ in the plane $z = 0$ with components u_x and u_y in the x- and y-directions, respectively, and the vorticity vector is directed normal to this plane with vertical component

$$\omega_z = \frac{\partial u_y}{\partial x} - \frac{\partial u_x}{\partial y}. \tag{4.2}$$

The two core parts of the vortex ring in this cross-sectional plane have positive and negative vorticity ω_z, respectively.

As already evident from the dye visualizations in figure 5, a typical feature of the evolution of the flow in this plane is the variation of the sizes of the core sections, which is opposite for the core parts on the inner and outer side of the curved ring

path. It will be shown now that this is a direct consequence of the Coriolis force acting on the flow field of the vortex ring. In the horizontal symmetry plane this force is given by $\boldsymbol{F_C} = \boldsymbol{u_2} \times 2\boldsymbol{\Omega}$ (per unit mass) and is directed orthogonal to the velocity vector $\boldsymbol{u_2}$ to the right. Figure 10(*a*) presents a vector plot of the initial velocity field of the vortex ring in the plane $z = 0$. For each of the velocity vectors a Coriolis force vector is plotted in figure 10(*b*). This Coriolis force vector plot demonstrates the presence of a mean force that deflects the motion of the vortex ring into a curved ring trajectory (in a clockwise sense). In addition, the orientations of the individual Coriolis force vectors indicate that the planar flow will be diverged from the outer core part (with anti-clockwise rotation) and converged towards the inner core part. In between the core parts the central axial flow of the vortex ring will be deflected to the right. This forced deflection of the flow generates a pressure gradient that partially opposes the effect of the Coriolis force. Only for steady inviscid flows in slow motion relative to a rotating system is the Coriolis force balanced completely by a pressure gradient, yielding a two-dimensional flow in "geostrophic equilibrium". In contrast, for the present three-dimensional flow the pressure forces do not cancel the deflecting Coriolis forces and in the subsequent evolution the flow structure changes according to the orientation of the force vectors in figure 10(*b*). As a consequence of the opposite forcing the outer core part (with positive ω_z) widens and the inner core part (negative ω_z) is squeezed, as observed previously in the dye visualizations.

On account of the incompressibility of the fluid, the squeezing of the inner core part of the vortex ring results in a local stretching of the fluid elements in a direction normal to the plane $z = 0$. The opposite happens at the widening outer core part where fluid elements are compressed along the same direction. The evolution of the vertical vorticity component ω_z of the planar flow field is affected by this local stretching and compressing of fluid elements. The relevant vorticity equation is obtained by taking the curl of the Navier–Stokes equation (3.1), yielding the equation

$$\frac{\mathrm{D}\omega_z}{\mathrm{D}t} = \omega_z \frac{\partial u_z}{\partial z} + \frac{1}{Ro}\frac{\partial u_z}{\partial z} + \frac{1}{Re}\nabla^2\omega_z, \tag{4.3}$$

while the other vorticity components vanish identically in the plane $z = 0$. In this equation u_z denotes the vertical velocity component that vanishes identically in the plane $z = 0$. The vertical gradient $\partial u_z/\partial z$ does not vanish and represents the local stretching ($\partial u_z/\partial z > 0$) and compressing ($\partial u_z/\partial z < 0$) of fluid elements along the vertical z-axis. According to (4.3) the vorticity ω_z changes by self-induced stretching and compression of relative vorticity (first term on right-hand side of (4.3)), induction of relative vorticity from the permanent background vorticity (second term), and viscous diffusion (third term). Since in the present simulation (with $Ro = 23$) the magnitude of the relative vorticity of the vortex ring is much larger than the uniform vorticity Ro^{-1} of the background rotation (both differing initially a factor $O(70)$), the first term on the right-hand side dominates the second term. Apart from viscous diffusion, the vorticity in the horizontal plane thus changes by self-induced stretching and compression of vortex lines of relative vorticity, which are initially circular lines along the toroidal axis of the vortex ring. At the squeezed inner core part vortex lines are vertically stretched and the negative vorticity ω_z in the horizontal plane increases (in an absolute sense); at the widened outer core part vortex lines are vertically compressed and the positive vorticity ω_z in the horizontal plane decreases. It is stressed that, although the induction of relative vorticity from the permanent background vorticity is of minor importance in these processes, the rotation of the system affects the vorticity dynamics of the flow indirectly by the opposite forcing

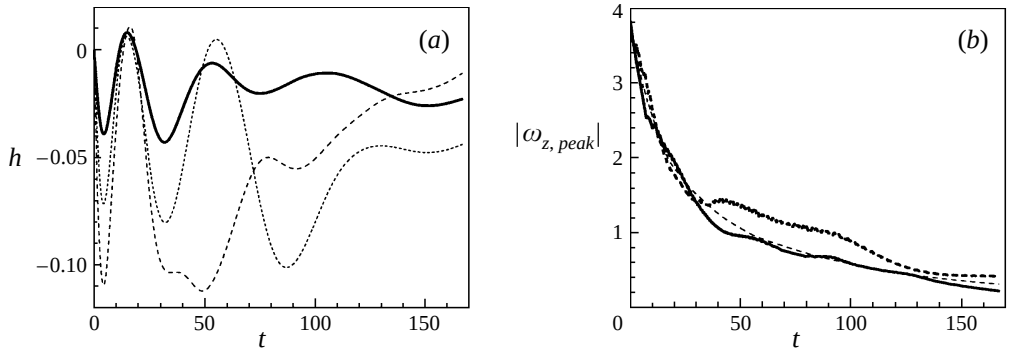

FIGURE 11. (*a*) Time evolution of the helicity h (computed only for the upper ring half) for three different Ro-values ($Re = 900$): $Ro = 23$ (solid line), $Ro = 12.6$ (dotted line) and $Ro = 8.2$ (dashed line). (*b*) Time evolution of the absolute values $|\omega_{z,peak}|$ of the peak vorticities in both core centres for $Ro = 23$ and $Re = 900$: positive peak (thick solid line) and negative peak (thick dashed line); decay of peak vorticity by viscous diffusion (without background rotation and $Re = 900$) is included for reference (thin dashed line).

of the vertical core parts of the vortex ring owing to Coriolis forces. Note that the induction of relative vorticity ω_z from the background vorticity might become important at later times, when the magnitude of the vorticity in the ring core has been decreased by viscous diffusion, or in simulations with increased background rotation.

The squeezing and widening of the core sections will drive a mass flow from one side of the vortex ring (the squeezed side) towards the other side. An easy way to verify the presence of such a flow is by computing the helicity $h = \int_V \boldsymbol{\omega} \cdot \boldsymbol{u} \, \mathrm{d}V$ over the volume V of the computational domain. In fact, the mass flow has to follow the toroidal axis of the ring and, since the flow direction is opposite to the vorticity vector, the helicity has to be negative. Of course this is because the evolution of only one half of the vortex ring is computed (see figure 2); in the complementary ring half the direction of the flow is in the same sense as that of the vorticity and the helicity is positive. The total helicity of the ring is thus zero, as one should expect from the presence of the horizontal symmetry plane. In figure 11 (*a*) the time evolution of the helicity of one ring half is shown for several cases with different Ro-values. For all simulations the helicity is on the average indeed negative, although oscillations are exhibited whose amplitudes depend on the Rossby number. These oscillations are due to the opposite squeezing and widening of the vertical ring core parts that, as explained in the previous paragraph, create a differential vorticity along the toroidal axis of the ring and induce, in turn, Kelvin waves (see e.g. Saffman 1992). In figure 11 (*b*) the time evolution of the absolute values $|\omega_{z,peak}|$ of the peak vorticities in both core centres are plotted for a simulation with $Ro = 23$. It shows the alternating differences between the vorticity peak in the outer core part (positive vorticity) and in the inner core part (negative vorticity) before $t \simeq 30$, in agreement to the oscillations in the helicity. The viscous decay of the peak vorticity in a simulation without background rotation is included for reference. After $t = 30$, small oscillations in the peak values are still observable, but now the negative peak always exceeds the positive peak in absolute value. Apparently, the stretching of the inner core part is enhanced by a secondary mechanism, but this will be addressed in the next subsection. For the moment, attention is focused on the formation of the Kelvin waves.

The mechanism by which Kelvin waves develop in vortices with variable cross-

sections can be summarized as follows: consider a straight vortex with constant circulation Γ, the vorticity $\bar{\omega}$ being uniformly distributed over a circular core with radius a. The tangential velocity u_ϕ in the core is sustained by a radial pressure force directed towards the vortex axis, as expressed in non-dimensional terms by

$$\frac{\partial p}{\partial r} = \frac{{u_\phi}^2}{r}, \tag{4.4}$$

according to which the pressure at the core axis is lower than at the core boundary. Suppose this vortex is locally perturbed, hence the core radius is not uniform along the axis of the vortex. On account of the conservation of circulation along the vortex the vorticity in the core is increased in regions where the core is narrow and the vortex rotates faster locally. Following (4.4), this enhanced swirling flow induces an additional reduction of the pressure at the core axis. Oppositely, in regions where the core is wide the vorticity is locally reduced and the vortex rotates slower, corresponding to a relatively higher pressure at the axis. This pressure gradient *along* the vortex axis causes an axial flow from wide core sections of high pressure towards narrow core sections of low pressure, thus tending to cancel the local variations of the core size. The restoring effect of this axial pressure force is responsible for the excitation of waves, travelling along the vortex axis.

The propagation of axial waves on rectilinear vortices was first studied by Thomson (1880) using a linear theory. Recently, in several papers this theory has been extended to more general vortex configurations (see e.g. Moore & Saffman 1972; Lundgren & Ashurst 1989) and the effects of viscosity and nonlinear terms have been examined by direct numerical simulations (see e.g. Verzicco, Jiménez & Orlandi 1995). For the present study, however, a thorough analysis of these waves is difficult, because of the complexity of the flow and the additional effect of the Coriolis force. It is well-known (Batchelor 1967, p. 555) that the Coriolis force might also act as a restoring force, that tends to eliminate local flow deformations by exciting waves. Therefore, to examine the nature of the observed oscillations in the helicity of the flow a series of simulations have been performed in which the Rossby number was varied. The results of these simulations are plotted in figure 11 (*a*). It is clear that initially the period of the oscillations is independent of the Rossby number, which proves that the oscillations are truly Kelvin waves. At later times the oscillation period increases and the increase is not the same for all the cases. In a very simple approach this increase can be explained using the expression for the group velocity $c_g \simeq 0.417\ \bar{\omega}a$ of long axisymmetric Kelvin waves on a uniform columnar vortex† (see Saffman 1992, p. 231). From this expression it is found that the group velocity of these waves varies proportionally to the vorticity in the vortex. As seen in figure 11 (*b*), during the evolution of the vortex ring in the rotating environment the vorticity in the ring core decays substantially by diffusion, implying a reduction of the group velocity of the waves and hence an increase in the oscillation period. This is confirmed by figure 11 (*a*), although the increase of the period is not the same for all the cases, since the amount of diffusion depends on the details of the flow structures which change with the Rossby number.

Some details of the complicated vortex dynamics can be reconstructed from the vorticity cross-sections shown in figure 12. To better appreciate the deformations

† Using the initial mean values $\bar{\omega} = 2$ and $a = 0.4$ yields $c_g = 0.33$. The wave propagates back and forth along half of the vortex ring toroidal axis, hence the total distance travelled in one period is $2\pi R = 6.3$, for $R = 1$ initially. The initial oscillation period is then $2\pi R/c_g = 19$, comparable to the period of the first oscillation in figure 11 (*a*).

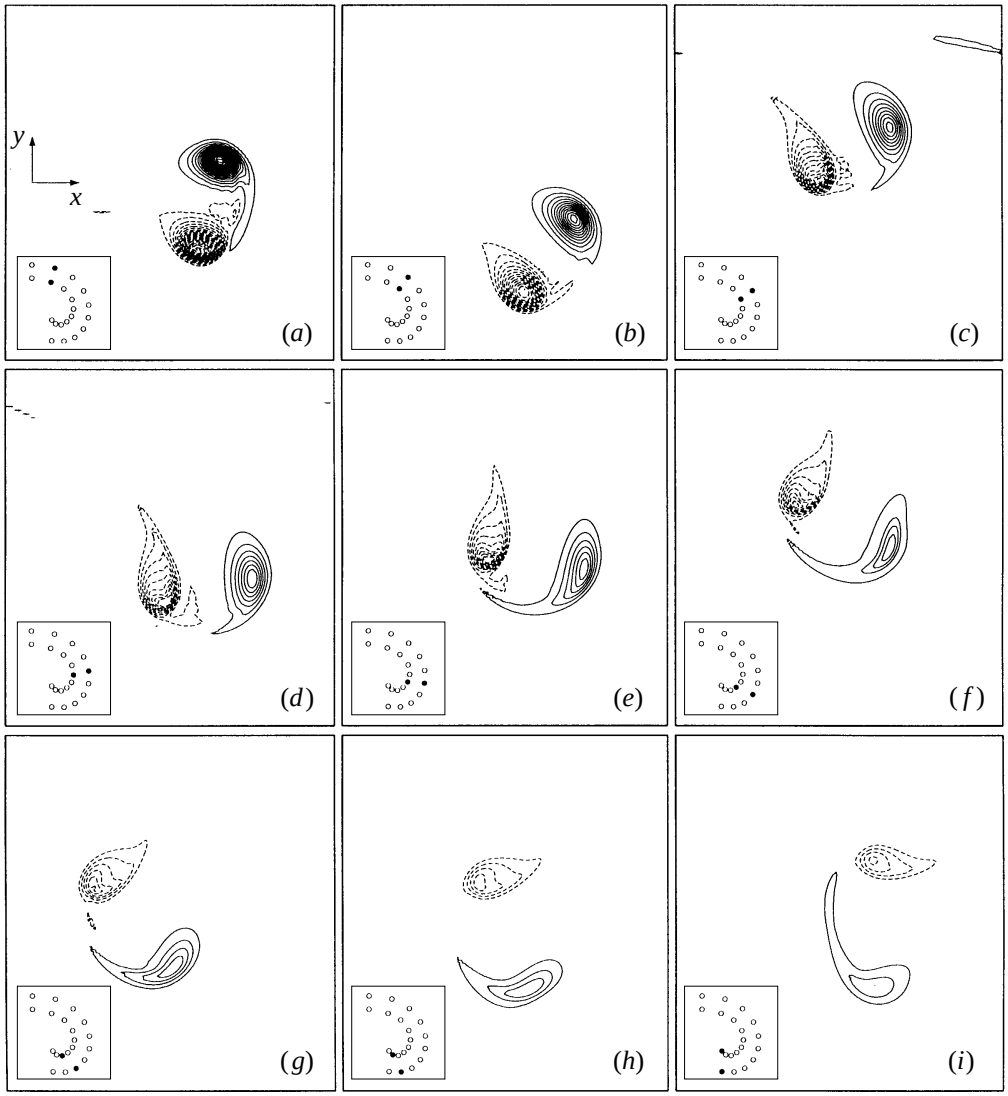

FIGURE 12. Contour plots of relative vorticity ω_z in the horizontal symmetry plane $z = 0$ of the vortex ring, obtained from a numerical simulation with $Ro = 23$ and $Re = 900$: (*a*) $t = 17$, (*b*) $t = 33$, (*c*) $t = 50$, (*d*) $t = 67$, (*e*) $t = 83$, (*f*) $t = 100$, (*g*) $t = 117$, (*h*) $t = 133$, (*i*) $t = 150$. Contour increments $\Delta\omega_z = \pm 0.1$, minimum contour level at $|\omega_z| = 0.1$; solid lines denote positive values and dashed lines negative values. The insets show the trajectories of the core centres: the instantaneous position of the vortex ring in each panel is denoted by black dots.

occurring in the vortex core, each panel in figure 12 is a blow-up of the small region occupied by the vortex ring. To get some feeling for the relative positions of these panels in the trajectory of the vortex ring, insets are provided showing the complete ring trajectory with the instantaneous ring positions denoted explicitly. The shrinking and widening of the core parts, already observed in the dye-visualization experiments, is confirmed by the vorticity contour plots of figure 12, even though additional features are observed. In front of the outer core part (positive vorticity ω_z) vorticity filaments are seen to be formed. The filaments are strained towards the opposite core part,

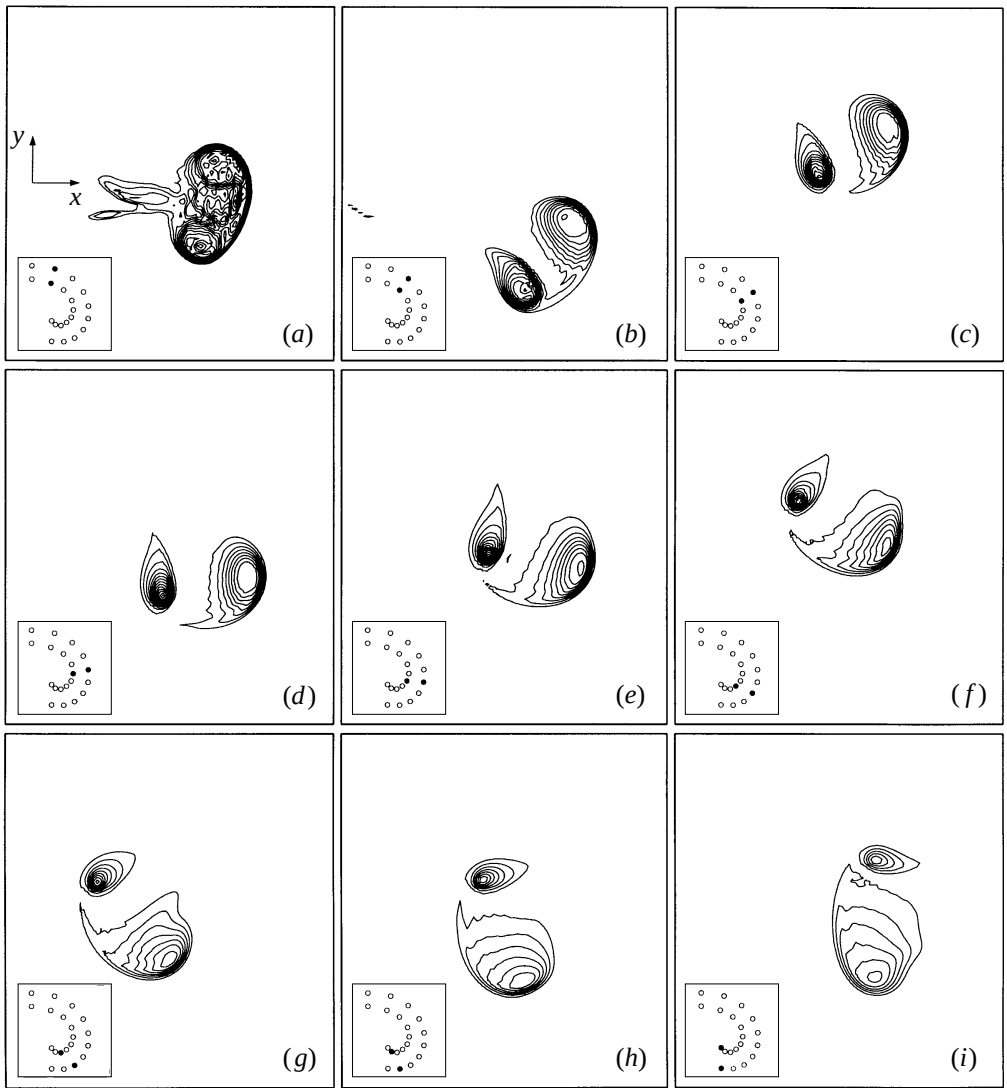

FIGURE 13. Contour plots of passive scalar concentration C in the horizontal symmetry plane $z = 0$ of the vortex ring, obtained from a numerical simulation with $Ro = 23$ and $Re = 900$: (*a*) $t = 17$, (*b*) $t = 33$, (*c*) $t = 50$, (*d*) $t = 67$, (*e*) $t = 83$, (*f*) $t = 100$, (*g*) $t = 117$, (*h*) $t = 133$, (*i*) $t = 150$. Contour increments $\Delta C = 0.1$; minimum contour levels: (*a–c*) $C = 0.25$, (*d*) $C = 0.2$ and (*e–i*) $C = 0.15$. The insets show the trajectories of the core centres: the instantaneous position of the vortex ring in each panel is denoted by black dots.

upon which they rapidly disappear owing to ordinary diffusion and cross-diffusion with oppositely signed vorticity. A similar formation of filaments was also observed in dye-visualization experiments (figure 5*d*) and is also seen in the contour plots of the passive scalar distribution (figure 13). These concentration plots also clearly reveal the continuous accumulation of scalars in the outer core part due to the azimuthal mass flow previously discussed. It is emphasized that the comparison between figures 12 and 13 is useful to better appreciate analogies and differences between vorticity and passive scalars due to the absence of vortex stretching and the reduced diffusivity of the latter.

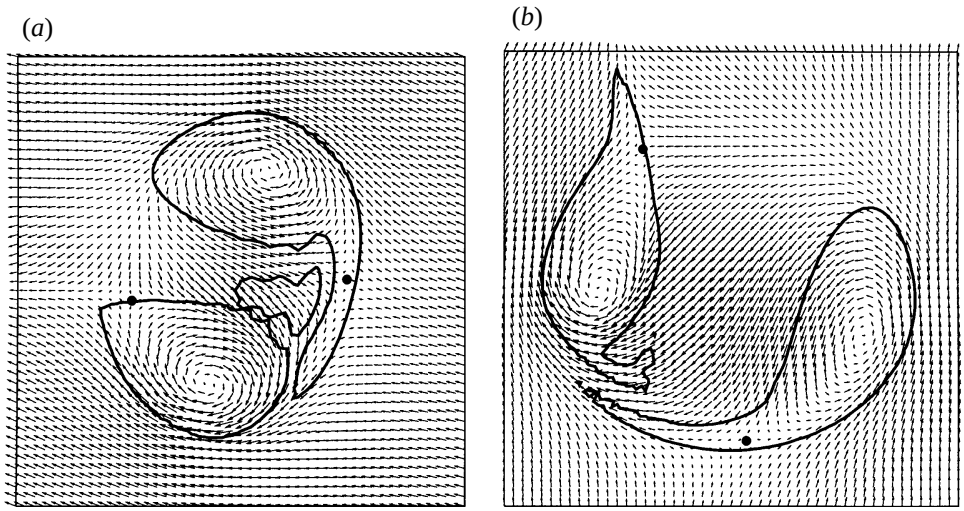

FIGURE 14. Velocity vector plots showing the velocity fields at $t = 17$ (a) and $t = 83$ (b) relative to a frame rotating instantaneously with the vortex ring. The positions of the shifted stagnation points are indicated by black dots. Contour lines at $|\omega_z| = 0.1$ show the stripping of vorticity from the boundary of the vortex core ($Ro = 23$ and $Re = 900$, cf. figure 12 a, e).

The reason for the formation of filaments stripped from the outer core part lies in the strain experienced by the vortex ring during its motion. This is easily verified by inspecting the velocity field of the vortex ring relative to a frame rotating instantaneously with the vortex itself. The construction of such a rotating frame is based on the observation (see § 4.2) that the vortex ring rotates with a constant angular velocity, opposite to the rotation Ω of the table. The decaying speed U of the vortex ring determines the radius of curvature R_c of the curved trajectory (see (4.1)) and the centre of the co-rotating frame is then located at the local centre of curvature.

The flow relative to such a co-rotating frame is shown in figure 14 as a velocity vector plot, with the vorticity contours $\omega_z = \pm 0.1$ showing the accompanying deformation of the boundary of the vortex core. The deflection of the relative flow due to Coriolis forces is clearly seen between the vortex core parts. As a result of this deflection, the stagnation point (marked by a black dot) at the front of the vortex ring is slightly shifted towards the outer core part†. When this point enters the boundary of the vortex core, a thin filament of vorticity is stripped and advected by the local strain flow, indicated by the adjacent velocity vectors. The position of the shifted stagnation point relative to the vortex ring varies in time, probably due to the presence of the Kelvin waves, and hence the stripping of the vortex core is not continuous, as was also found in the experiment and in the numerical simulation. Incidentally, it is noted that, even though vortex filaments in the front of the ring are preferentially peeled from the outer core part, there are some instants ($t = 33$ and $t = 67$ in figure 12) during which filaments are also peeled from the inner core part. These times correspond to the negative peaks of the helicity (figure 11 a), giving further support to the idea that the oscillations induced by Kelvin waves modify the location of the frontal stagnation point, causing the filament formation to be intermittent.

† In the absence of the background rotation this stagnation point is located at the central axis of the vortex ring.

Similarly to the frontal stagnation point, the stagnation point at the rear of the vortex ring is also shifted, but in this case towards the inner core part. The deformation of this core part also results from the position of the stagnation point, which in figure 14 is located at the border of the core section. The strain flow surrounding the stagnation point then causes the observed elongation of this core part.

The shedding of vortex filaments from the ring core causes the vortex ring to gradually weaken in time until hardly any vorticity is left in the structure ($t = 150$ in figure 12). This results in a rapid decrease of the translation velocity U of the vortex ring, faster than solely viscous decay as evidenced in figure 8. Also, since the vortex stripping is directly related to the deflection of the flow relative to the vortex ring, this phenomenon will be enhanced when the rotation rate is increased. This is again confirmed by the results of figure 8 and by the consequently more strongly curved trajectories of figure 7.

4.4. *Three-dimensional flow structure*

In order to get a complete picture of the ring dynamics, its three-dimensional structure should be investigated. Since it is difficult to gain insight into the three-dimensional flow from laboratory experiments, the further investigation is mainly based on numerical simulations.

One specific feature, observed from the simulations, is the creation of a secondary vortex that extends as a horizontally elongated tail behind the main vortex ring. This is shown in figure 15 by plotting perspective views of vorticity magnitude iso-surfaces. Indeed, a similar structure also appeared in the laboratory experiments (see figure 5 *d*) as a thin filament of dye between and behind the dyed core parts, although it was not self-evident from the visualizations that this dye filament indicated the presence of a tail vortex.

The tail vortex is located near the centre of the vortex ring, slightly above the mirror plane of the flow and the vorticity in this vortex points away from the vortex ring, according to the sense of rotation indicated in figure 15 (*a*). Because of the symmetry of the flow, there is a similar vortex below the mirror plane with oppositely signed vorticity and both vortices compose a vortex pair. To verify that the formation of this vortex pair does not depend upon the numerical boundary conditions imposed at the plane $z = 0$, a simulation of a complete vortex ring has been performed. Figure 16 shows the pair of elongated vortices behind the vortex ring for this simulation. This vortex pair propagates by mutual propulsion perpendicularly to its orientation along the horizontal plane, as indicated in figure 15 (*c*). Note that in the horizontal plane $z = 0$ the flow associated with this vortex pair agrees with the deflection of the flow near the centre of the vortex ring observed in figure 14 (*a*).

The appearance of such a strong vortex pair behind the ring could hardly be expected without the results of the numerical simulation. Once this structure is found, however, it is necessary to explain the mechanism of its formation. The creation of the vortex pair must result from stretching and tilting of vortex lines. Taking advantage of the initially symmetric structure of the vortex ring, more insight in the tail-formation might be gained by examining the vorticity transport equation attentively. In this analysis another interpretation will be obtained for the curved trajectory of the vortex ring.

Taking the curl of the Navier–Stokes equation in (3.1) gives the vorticity equation:

$$\frac{\mathrm{D}\boldsymbol{\omega}}{\mathrm{D}t} = (\boldsymbol{\omega}\cdot\nabla)\boldsymbol{u} + \frac{1}{Ro}(\boldsymbol{k}\cdot\nabla)\boldsymbol{u} + \frac{1}{Re}\nabla^2\boldsymbol{\omega}. \tag{4.5}$$

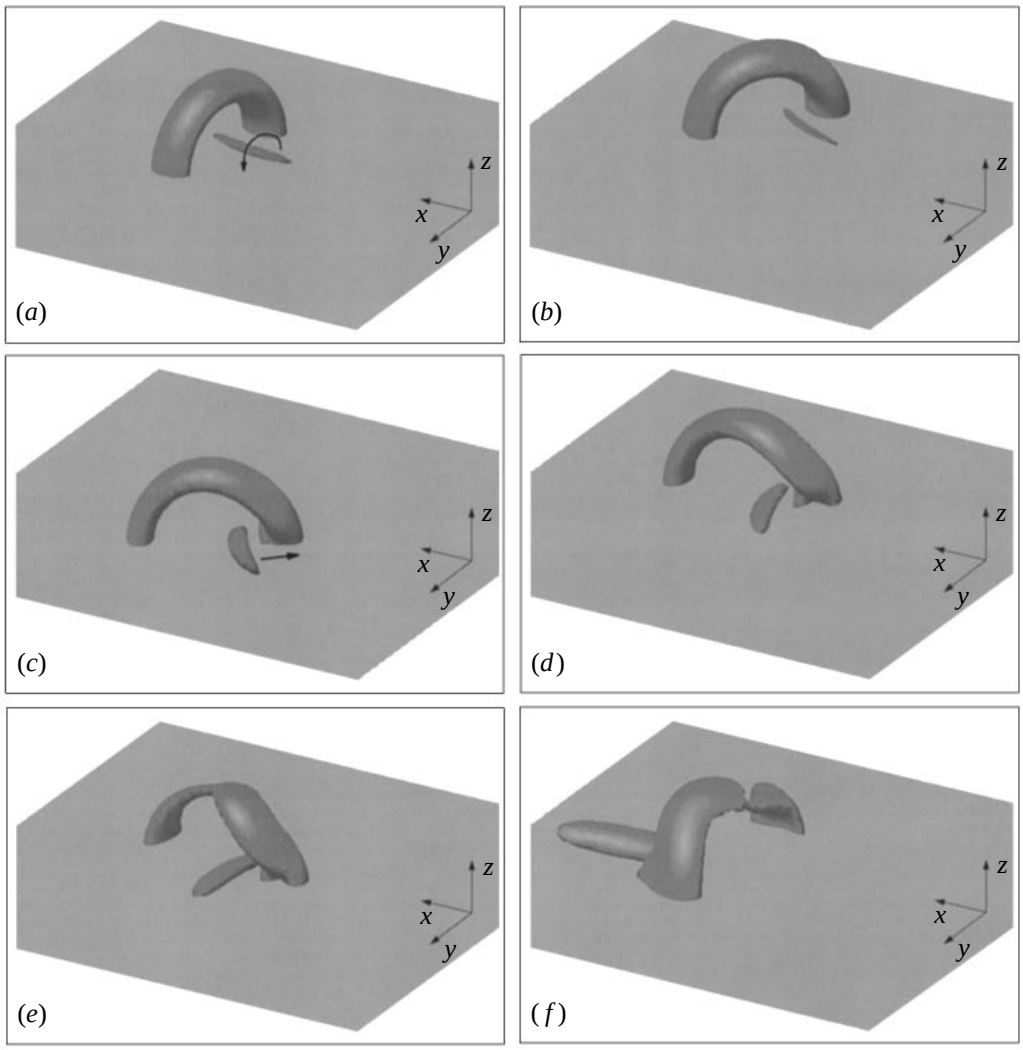

FIGURE 15. Perspective views of the evolution of the vortex ring structure as represented by isosurfaces of *relative* vorticity, obtained from a simulation with $Ro = 23$ and $Re = 900$. The curved arrow in (a) indicates the sense of rotation in the tail vortex, which propagates in a horizontal plane in the direction of the arrow in (c). The vortex ring is mainly viewed from the rear side to show the relative position of the tail vortex; the initial propagation of the vortex ring is in the direction of the positive x-axis. Isosurfaces $|\boldsymbol{\omega}|$ plotted for each moment at half the maximum value $|\boldsymbol{\omega}|_{peak}$: ($a$) $t = 17$, (b) $t = 33$, (c) $t = 50$, (d) $t = 67$, (e) $t = 83$, (f) $t = 150$.

The second term on the right-hand side acts as an additional source term by which relative vorticity is induced by the permanent rotation of the system. This mainly occurs in regions of the flow where the vertical gradient $(\boldsymbol{k} \cdot \nabla)$ of the velocity field is large. For the present flow this happens in planes where the vorticity in the core is perpendicular to the axis of rotation of the system, i.e. in the vertical plane through the centreline of the vortex ring. Note that in the case of zero background rotation all other terms in (4.5) are in balance for an axisymmetric vortex ring, so that any deviation from this structure now primarily results from the term proportional to $1/Ro$.

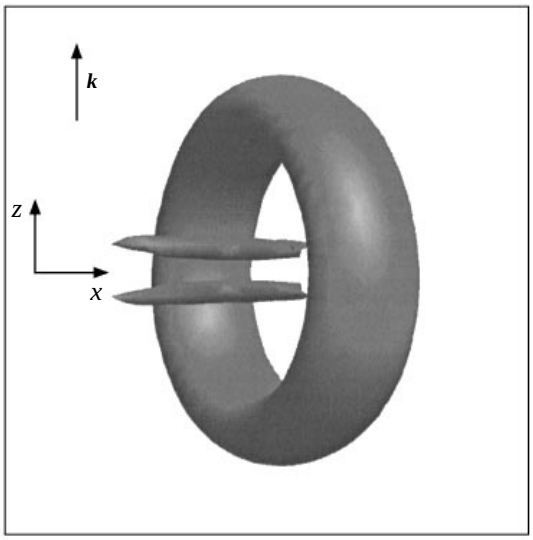

FIGURE 16. Perspective view from the side of the complete vortex ring structure as represented by an isosurface of *relative* vorticity, obtained from a simulation with $Ro = 23$ and $Re = 900$ at $t = 17$. The vortex ring propagates from left to right, two elongated counter-rotating vortices are observed extending behind the vortex ring. Isosurface $|\boldsymbol{\omega}|$ plotted at half the maximum value $|\boldsymbol{\omega}|_{peak}$.

Consider the flow in the vertical plane through the centreline of the vortex ring, slicing the horizontal parts of the ring core orthogonally. Initially, the flow in this plane is equal to the flow in the horizontal plane $z = 0$ examined in the previous subsection, owing to the axisymmetric structure of the initial vortex ring. One can thus think of the flow as presented in figure 10 (a) with now the x- and the z-axes oriented horizontally and vertically, respectively. The vorticity in the sections of the ring core is normal to this vertical plane and is thus directed parallel to the y-axis. Since the unit vector $\boldsymbol{k}$ points along the z-axis (hence $(\boldsymbol{k} \cdot \nabla) = \partial/\partial z$), the second term on the right-hand side of (4.5) describes the induction of relative vorticity components ω_x and ω_z at a rate proportional to $\partial u_x/\partial z$ and $\partial u_z/\partial z$, respectively. Direct inspection of the magnitude of the terms $\partial u_x/\partial z$ and $\partial u_z/\partial z$ has shown that the former is dominant (see figure 17 a, b). Since in the upper half of the vortex ring $\partial u_x/\partial z < 0$ in the main part of the cross-section, the induced axial vorticity component ω_x is negative. Of course, the same (with the gradient sign reversed) occurs in the lower half of the ring, implying the generation of positive ω_x. Near the ring centre these vorticity components strengthen due to self-induced vortex stretching, according to the component $\omega_x(\partial u_x/\partial x)$ in the term $(\boldsymbol{\omega} \cdot \nabla)\boldsymbol{u}$ on the right-hand side of (4.5). The contour plot of $\partial u_x/\partial x$ (figure 17 c) shows that $\partial u_x/\partial x > 0$ (vortex stretching) at the rear of the vortex ring and $\partial u_x/\partial x < 0$ (vortex compression) at the front side. It should be stressed that, although the analysis of the terms in figure 17 is performed only for $t = 0$, the same velocity gradients also appear at later times (with the x- and z-axes tilted according to the rotation of the vortex ring). As evidenced in figure 15, the toroidal structure of the main vortex ring does not change much.

Considering now the whole vortex ring one can think of the following mechanism for the formation of the tail vortices. To explain this it is necessary to introduce the absolute vorticity $\boldsymbol{\omega_a} = \boldsymbol{\omega} + (1/Ro)\boldsymbol{k}$ of the flow, representing the vorticity relative to an inertial (non-rotating) frame of reference. It can be shown (see Pedlosky 1987,

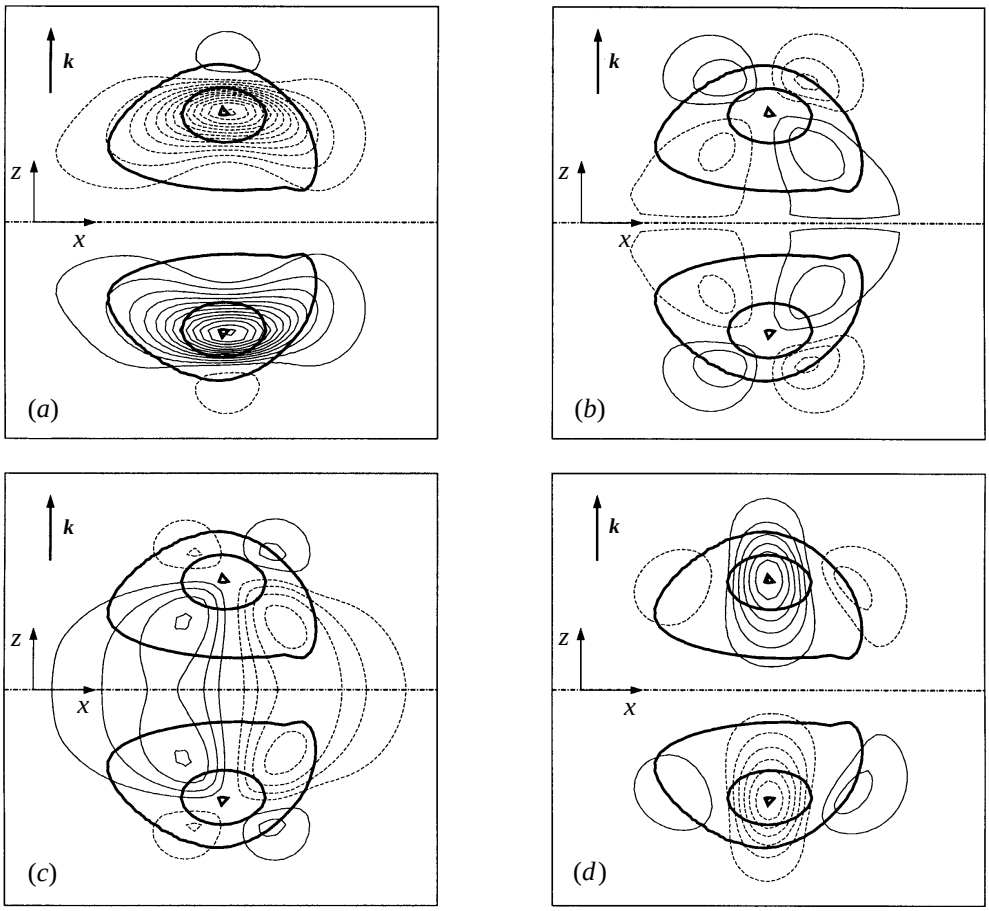

FIGURE 17. Contour plots of (*a*) $\partial u_x/\partial z$, (*b*) $\partial u_z/\partial z$, (*c*) $\partial u_x/\partial x$ and (*d*) $\partial u_z/\partial x$ in the vertical (x, z)-plane through the centre of the initial vortex ring. Solid lines denote positive values and dashed lines negative values, contour increments ± 0.1. The structure of the ring core is represented by several thick vorticity contour lines (levels $|\omega_y| = 0.1$, 1.0 and 2.0). The chain-dotted line is the trace of the horizontal symmetry plane of the flow on the cross-section of the vortex ring.

p. 34) that vortex lines of absolute vorticity $\boldsymbol{\omega}_a$ are advected with the flow as material lines (at least in the limit of inviscid flow according to Kelvin's theorem), a property that does not hold for vortex lines of relative vorticity $\boldsymbol{\omega}$. In the present flow, far from the vortex ring there is only the background vorticity due to the ambient rotation, oriented along the z-axis with non-dimensional magnitude $1/Ro$. The corresponding vortex lines of absolute vorticity are thus straight vertical lines. However, those vortex lines passing close to the vortex ring will be tilted according to the local velocity gradients in the flow field of the vortex ring, as shown in figure 18. The dominant terms are $\partial u_x/\partial z < 0$ in the upper ring half and $\partial u_x/\partial z > 0$ in the lower half, generating relative vorticity components $\omega_x < 0$ and $\omega_x > 0$, respectively. In the region behind the vortex ring the generation of negative ω_x in the upper ring half means that the vortex lines gain a negative slope and thus are tilted towards the vortex ring centre. Closer to the symmetry plane these tilted vortex lines are intensified by self-induced vortex stretching due to the gradient $\partial u_x/\partial x > 0$ in the flow field at the rear side of the vortex ring. This combination of vortex line tilting, induced by the

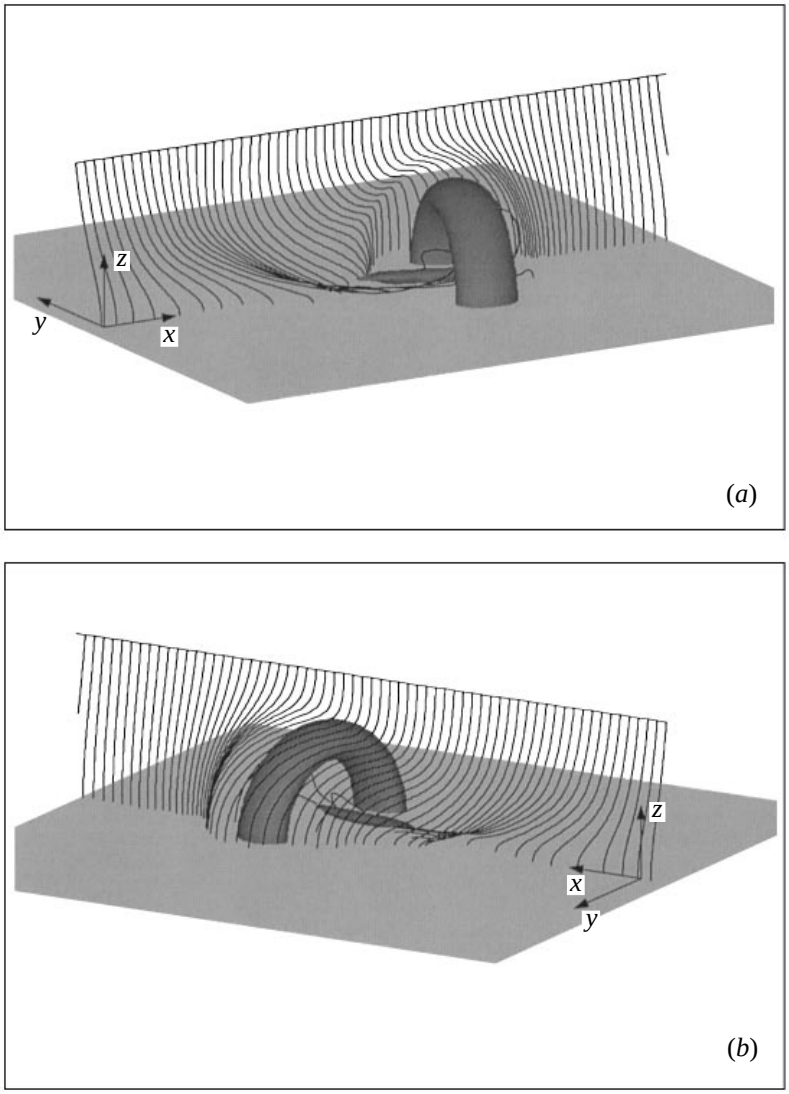

FIGURE 18. Two different perspective views taken from the rear side of the vortex ring at $t = 17$ through iso-surfaces of *absolute* vorticity $|\boldsymbol{\omega_a}| = 0.5|\boldsymbol{\omega_a}|_{peak}$ ($Ro = 23$ and $Re = 900$; cf. figure 15 *a*). Vortex lines of absolute vorticity are released from a single horizontal line (drawn in the figure) that represents the intersection of the horizontal plane $z = 2$ and the vertical (x, z)-plane through the centre of the initial vortex ring. Far from the vortex ring the vorticity in the vortex lines points vertically upwards; close to the vortex ring vortex lines are tilted and stretched due to local gradients in the velocity field of the vortex ring.

system rotation, and subsequent self-induced stretching results in the formation of the horizontally elongated tail vortex in the upper ring half (see figure 18 *a*). The vorticity in this tail vortex is in the direction of the negative x-axis. In the lower ring half (not shown in figure 18) the tilting of vortex lines behind the vortex ring results in vortex lines with a positive slope (generation of $\omega_x > 0$). One can imagine that these vortex lines are also deflected towards the centre of the vortex ring. In fact, the vortex lines in the upper ring half continue in the lower ring half and the tilting and stretching

processes are mirror-symmetric. Subsequent stretching of these tilted vortex lines at the ring centre yields a tail vortex in the lower ring half with vorticity pointing along the positive x-axis, hence opposite to the vorticity in the tail vortex in the upper ring half.

As mentioned above, these tail vortices form a vortex pair propagating towards the vertical core part on the inner side of the ring trajectory (as observed in figure 15), where they interfere with the local orthogonal vorticity in this core part. On the one hand, the circumferential flow associated with each leg of the vortex pair induces an additional stretching of the vorticity in this core part while, on the other hand, the vortex pair is curved by the main flow of the vortex ring. The increase of stretching induced by this vortex pair further enhances the squeezing of the vortex core and the differential vorticity along the toroidal axis of the vortex ring. As a result of this strong interaction with the tail vortices the ring core is locally distorted, as seen in figure 15 (*b–e*). This torsion is also reflected in the deformed shape of the negative vorticity contour lines near the core centre in figure 12.

It should be noted that in the upper half of the ring the vorticity vector in the tail vortex points in the opposite direction with respect to the local flow velocity, thus generating additional negative helicity. This contribution is already included in the data of figure 11 (*a*): the negative helicity must be attributed partly to the mechanism previously described (see § 4.3) and partly to the tail vortex. However, it has been checked by separation of these two contributions that the oscillatory behaviour is entirely due to Kelvin waves and the helicity contribution of the tail is always negative.

Returning to (4.5), a proper interpretation of the rotation term can give a different explanation of the curved ring trajectory. By rewriting the rotation term in (4.5) as

$$\frac{1}{Ro}(\boldsymbol{k}\cdot\nabla)\boldsymbol{u} \equiv \frac{1}{Ro}\boldsymbol{\omega}\times\boldsymbol{k} + \frac{1}{Ro}\nabla(\boldsymbol{k}\cdot\boldsymbol{u}), \tag{4.6}$$

it appears that the first term on the right-hand side is a pure rotation of pre-existing vorticity, while the second term is a transformation of background vorticity $(1/Ro)$ into relative vorticity due to the gradient of the velocity component parallel to $\boldsymbol{k}$. Recalling that $\boldsymbol{k}$ is oriented in the direction of the z-axis, the first term on the right-hand side describes a rotation of the vorticity vector $\boldsymbol{\omega}$ in the vortex ring core around this axis in clockwise direction. Since this tilting occurs at a rate $1/Ro$, a faster rotation of the ambient fluid will enhance the curvature of the ring trajectory, as confirmed by the results of figure 7. Although this approach demonstrates the curved motion of the vortex ring very nicely, the complete picture is more complicated. In fact, the rotation rate depends on the local angle between $\boldsymbol{\omega}$ and $\boldsymbol{k}$, which varies along the toroidal ring axis. In the vertical parts of the vortex ring $\boldsymbol{\omega}$ and $\boldsymbol{k}$ are either parallel or antiparallel and $\boldsymbol{\omega}\times\boldsymbol{k}$ vanishes identically. For the horizontal parts of the vortex ring the clockwise rotation around the z-axis means that the vorticity vector pointing initially parallel to the y-axis is gradually turned towards the direction of the x-axis. This tilting is counteracted by the component $(1/Ro)\partial u_z/\partial x$ in the second term on the right-hand side in (4.6) as follows. In the horizontal part of the vortex core in the upper ring half the vorticity has initially a negative component ω_y and this is turned into a negative component ω_x by the clockwise ring rotation. The second term in (4.6) describes the generation of ω_x at a rate proportional to $\partial u_z/\partial x$. As seen in figure 17 (*d*) this gradient is positive in the upper ring half, thus generating positive ω_x that partially opposes the negative ω_x due to the clockwise rotation. As a

consequence of these effects the vortex ring does not have a uniform rotation, leading to internal distortion of the vortex structure. Nevertheless, as shown in § 4.2, the vortex ring propagates with average rotation equal and opposite to the background rotation $1/(2Ro)$ of the system.

Before coming to the conclusions one further comment should be made about figure 15. The vorticity iso-surfaces in this figure have been drawn using for each time half the value of the instantaneous peak vorticity. As can be seen from figure 11 (*b*), however, the peak vorticity undergoes a substantial decrease in time owing to ordinary viscous diffusion and to the peeling processes described in § 4.3. This implies that the vortex ring of figure 15 at $t = 150$ is in fact a very weak structure even though it preserves its toroidal topology. This result agrees with the laboratory experiments in which at the end of the ring evolution a compact blob of dyed fluid with hardly any motion was observed.

5. Conclusions

In this paper the dynamics of a vortex ring that propagates perpendicularly to the axis of a uniformly rotating fluid has been investigated. The interaction between the permanent vorticity of the rotating fluid and the ring vorticity yields a comprehensive example of the complex dynamics of localized vorticity distributions in rotating flows. Owing to the initially 'simple' structure of the vortex ring, the analysis of the development of the flow can be pursued in detail, yielding a thorough insight into the induction and dynamics of relative vorticity in rotating systems. The investigation was based both on laboratory experiments and on numerical simulations, which were used as complementary tools.

Flow visualization experiments have shown that the vortex ring propagates in the rotating system along a curved path, being deflected clockwise if the system rotates anti-clockwise. A similar behaviour was observed in laboratory experiments by Taylor (1917, 1921), though his experiments were only aimed at demonstrating the analogy with the motion of a solid sphere in a rotating fluid. In Taylor's papers, neither measurements of the ring trajectory nor details on the evolution of the vortex structure were reported. In the present study the ring trajectory has been measured by following the dyed core patches in an illuminated cross-section of the vortex ring. The trajectory has a spiral shape in the rotating frame, while the vortex ring maintains its orientation with respect to the laboratory frame. Another typical feature of the flow, observed from flow visualizations, is the variation of the size of the core cross-sections: the section along the inner side of the trajectory gradually shrinks while the other section expands in time.

Examination of the velocity field in the horizontal symmetry plane of the flow shows that the flow near the ring centre is strongly deflected, owing to the action of the Coriolis force. Also the flow around the vortex cores is deflected, forcing both core sides oppositely. One side of the core expands while the other side contracts and these processes are accompanied by compression and stretching of vortex lines, respectively. Owing to this local forcing of the vortex core inertial waves, similar to Kelvin waves along a rectilinear vortex, are excited, travelling along the toroidal axis of the ring. The increase in time of the period of these waves could be explained by applying the theoretical results for the group velocity of Kelvin waves along an infinitely long vortex: the group velocity of these waves is proportional to the vorticity of the vortex. In the case of the vortex ring the vorticity decreases mainly by viscous diffusion, resulting in a decaying group velocity and hence longer

periods for the wave motion along the ring core. The deflection of the flow around the vortex ring also caused the front and rear stagnation points to be shifted. In particular, the front stagnation point was preferentially moved towards the core part on the outer side of the ring trajectory, while the opposite happened for the rear stagnation point moving towards the inner core part. The local strain around these points led to stripping of vorticity filaments from the vortex ring, thus producing a progressive weakening of the vortex structure leading to complete depletion. This phenomenon is confirmed by the time evolution of the translation velocity of the vortex ring (figure 8), which decays in time at a rate faster than in the non-rotating case.

To gain more insight into the evolution of the three-dimensional structure of the vorticity field, the results from the numerical simulations were analysed in detail. It has been proved, by checking the trajectory and velocity of a vortex ring both in a fluid at rest and relative to a rotating fluid, that the numerical simulations mimic the laboratory experiments very well. Furthermore, the evolution of the flow in a horizontal cross-sectional plane through the vortex ring has been compared with the video images obtained from dye-visualization experiments. Despite the restriction that the advection of passive scalars could only be simulated at disproportionately low Schmidt numbers, the gradual deformations on each vertical core part of the vortex ring were readily reproduced.

A specific feature of the flow, observed by examining the three-dimensional structure of the vortex, is the formation of a horizontally extending vortex pair at the tail. A detailed analysis has shown that this vortex pair is created by turning and stretching of vortex lines by the main vortex ring. This process is initiated by the induction of relative vorticity due to the rotation of the system, but the subsequent evolution into an elongated vortex pair is dominated by the main flow field of the vortex ring. The vortex pair propagates by its self-induced motion in a horizontal plane towards the shrinking side of the main vortex ring, increasing the local stretching there and thus enhancing the squeezing of this vertical core part. As a result the vortex core is locally distorted.

Most of the experiments and simulations were performed at a relatively low rotation rate of the system, i.e. $Ro \geqslant 8$. In these cases the development of deformations on the main vortex structure could readily be followed in time and a thorough analysis of the evolution of the vorticity field was possible. A few simulations have been done with $Ro < O(1)$. The coherent structure of the vortex ring is then rapidly destroyed by the strongly enhanced stretching and turning of vortex lines. Moreover, induction of relative vorticity is then no longer restricted to a region of the flow close to the vortex ring, but it takes place over the whole flow domain, probably radiating inertial waves. These results, however, cannot be considered as reliable, mainly for two reasons: if inertial waves were radiated the limited size of the computational domain and the periodic conditions on the lateral boundaries would then no longer be suitable for studying the preferably unbounded flow field. In addition, as mentioned in § 3.3, the rotation of the system affects the whole flow evolution, and so also the generation of the vortex ring. For the range of Rossby numbers investigated in the present paper it was known from previous experiments that a vortex ring was formed initially, and therefore an axisymmetric vortex ring could be used as initial condition. In contrast, for higher rotation rates this is not known and it would seem more appropriate to use a numerical set-up as in Verzicco *et al.* (1996), where the initial vortex structure was generated by injection of a finite amount of fluid through an orifice.

This research was partially carried out during a visit of one of the authors (R.V.) to the Fluid Dynamics Laboratory in Eindhoven, which was financially supported by the Dutch Organization for Scientific Research (NWO). The authors are indebted to Professor P. Orlandi and Dr G. F. Carnevale for discussion of the results and gratefully acknowledge the anonymous referees for their valuable comments on an earlier version of the paper. R.V. acknowledges the support by grants MURST 60% (Ministero dell'Università e della Ricerca Scientifica e Tecnologica) and ASI.

Appendix

In this Appendix the forces that are exerted on a solid object that propagates perpendicularly to the axis of a rotating fluid are discussed. Attention is focused to two special cases, i.e. the forces on a solid sphere and on a solid cylinder. These cases typically illustrate the effect of the rotation of the fluid on either a three-dimensional or a two-dimensional flow. Taylor (1917) discussed the forces that are exerted on the sphere, which are responsible for the deflection of the sphere's trajectory from a straight line. The mathematical derivation of the expressions for these forces was performed by Proudman (1916). For completion of the discussion in § 4.2 the main results of these studies are summarized here briefly, emphasizing the difference in the force balance exerted on a cylinder and on a sphere.

Consider a homogeneous solid object (either a cylinder or a sphere) of mass M placed in a fluid that rotates with angular velocity Ω. The object moves steadily in a prescribed motion with velocity U in a direction perpendicular to the rotation vector. In addition to the pressure and viscous forces that are exerted on the object, in the case of zero rotation, the object also experiences two inertial forces that directly originate from the applied system rotation: (i) a centrifugal force $M\Omega^2 D$ acting through the centre of gravity $\mathscr{C}$ of the object, pointing away from the centre of rotation (D is the distance of $\mathscr{C}$ from the centre of rotation), (ii) a Coriolis force $2M\Omega U$ perpendicular to the direction of the velocity U of the centre $\mathscr{C}$, directed to the right if the rotation of the fluid is anti-clockwise (see figure 19).

Furthermore, an additional pressure force is exerted by the surrounding flow on the boundary of the object. This net pressure force results from the various inertial forces (i.e. centrifugal and Coriolis forces) related to the system's rotation that act on the flow around the moving object. Expressions for the components of this pressure force had been derived by Proudman (1916) and applied by Taylor (1917). For a vertical cylinder with horizontal cross-sectional area A, extending over the whole fluid depth, these components per unit axial length consist of: (i) a force $M_F\Omega^2 D$ acting through $\mathscr{C}$ towards the centre of rotation and (ii) a force $2M_F\Omega U$ acting at $\mathscr{C}$ perpendicularly to U to the left (see figure 19). Here, $M_F = \rho A$ is the mass per unit length of the region of the fluid occupied by the solid object, ρ being the density of the fluid. If the cylinder and the fluid have the same density, all forces that are related to the rotation of the system cancel and the cylinder moves along a straight path, as if the rotation were absent.

An important property of any two-dimensional flow (u, v) in a rotating fluid, related to this result, is the possibility of rewriting the components of the Coriolis acceleration $(-2\Omega v, 2\Omega u)$ in the Navier–Stokes equation in terms of the gradient of a scalar function. Describing the two-dimensional flow by a stream function ψ, defined by

$$u = \frac{\partial \psi}{\partial y} \quad \text{and} \quad v = -\frac{\partial \psi}{\partial x}, \tag{A 1}$$

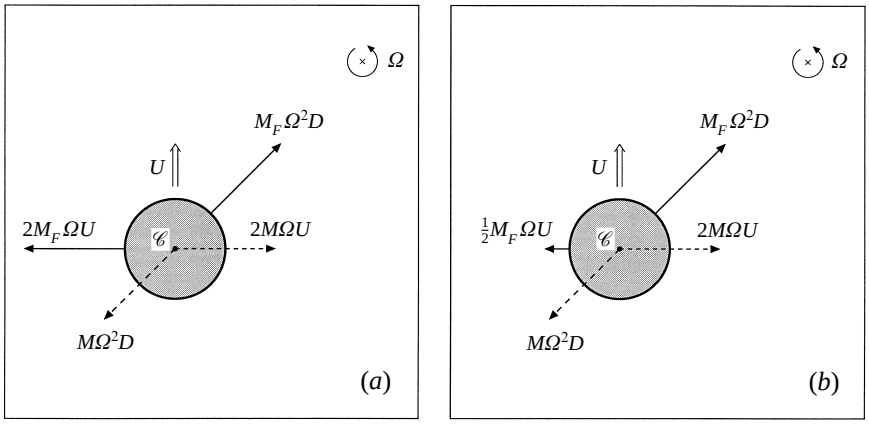

FIGURE 19. Additional forces exerted on a cylinder (*a*) and a sphere (*b*) due to the system's rotation (top view, the centre of rotation is marked by a cross at the top right corner, an arrow indicates the anti-clockwise rotation of the system.) Centrifugal and Coriolis forces (dashed arrows) act at the centre of gravity $\mathscr{C}$ of the object, while competing components of fluid pressure forces (solid arrows) are exerted on the solid's surface. For the sphere the resultant force is directed perpendicular to its motion to the right, deviating its path from a straight line. U is the velocity of the object, M is the mass of the object, M_F is the mass of the fluid region occupied by the object, D is the distance of the centre $\mathscr{C}$ of the object from the rotation centre and Ω is the system's rotation rate.

the expression $2\Omega\psi$ is found for this scalar function. This implies that a reduced pressure field $p' = p + 2\Omega\psi\rho$ can be defined that, in addition to the centrifugal force, also includes the Coriolis force on the fluid flow. In terms of the pressure p' the Navier–Stokes equation describing the flow relative to a rotating frame of reference reduces to its formulation in an inertial frame and hence the two-dimensional flow in the rotating system is not affected by the rotation.

For a sphere of volume V, however, the flow generated around it is essentially three-dimensional and the forces due to fluid pressure are insufficient to cancel the inertial forces on the sphere. The mathematical derivation of the total pressure force on a sphere is rather complicated and the results obtained by Proudman (1916) will be used, who derived the following expressions for the components of the pressure force: (i) a force $M_F\Omega^2D$ directed towards the centre of rotation and (ii) a force $\frac{1}{2}M_F\Omega U$ perpendicular to U to the left (see figure 19). In this case $M_F = \rho V$ is the total mass of the region of the fluid occupied by the solid object, ρ being the density of the fluid. If the sphere and the fluid have the same density, the component of the resultant force perpendicular to the sphere's motion does not vanish and the sphere is compelled to move along a curved trajectory, its path being deflected to the right.

A special situation occurs when the sphere is moved very slowly and the system rotates at a considerable speed. According to Proudman's theorem any slow steady motion relative to the rotating system is then two-dimensional. Experiments performed by Taylor (1923) have shown that for the sphere also a steady two-dimensional flow is established. In fact, he had observed that a cylinder of fluid of the same diameter as the sphere moves with the sphere and acts towards the rest of the fluid as if it were a solid cylinder. Such a cylinder of fluid, accompanying an object moving in a rotating system, is commonly called a 'Taylor column'.

REFERENCES

Batchelor, G. K. 1967 *An Introduction to Fluid Dynamics*. Cambridge University Press.

Dalziel, S. 1992 *DigImage. Image Processing for Fluid Dynamics*. Cambridge Environmental Research Consultants Ltd.

Kim, J. & Moin, P. 1985 Application of a fractional-step method to incompressible Navier–Stokes equations. *J. Comput. Phys.* **59**, 308–323.

Lundgren, T. S. & Ashurst, W. T. 1989 Area-varying waves on curved vortex tubes with application to vortex breakdown. *J. Fluid Mech.* **200**, 283–307.

Métais, O., Flores, C., Yanase, S., Riley, J. J. & Lesieur, M. 1995 Rotating free-shear flows. Part 2. Numerical simulations. *J. Fluid Mech.* **293**, 47–80.

Moore, D. W. & Saffman, P. G. 1972 The motion of a vortex filament with axial flow. *Phil. Trans. R. Soc. Lond.* A **272**, 403–429.

Orlandi, P. 1990 A numerical method for direct simulation of turbulence in complex geometries. *Annual Research Briefs, 1989. Ames Center for Turbulence Research*, pp. 215–229.

Pedlosky, J. 1987 *Geophysical Fluid Dynamics*, 2nd Edn. Springer.

Proudman, J. 1916 On the motion of solids in liquids possessing vorticity. *Proc. R. Soc. Lond.* A **92**, 408–424.

Saffman, P. G. 1992 *Vorticity Dynamics*. Cambridge University Press.

Taylor, G. I. 1917 Motion of solids in fluids when the flow is not irrotational. *Proc. R. Soc. Lond.* A **93**, 99–113.

Taylor, G. I. 1921 Experiments with rotating fluids. *Proc. R. Soc. Lond.* A **100**, 114–121.

Taylor, G. I. 1923 Experiments on the motion of solid bodies in rotating fluids. *Proc. R. Soc. Lond.* A **104**, 213–218.

Thomson, W. 1867 On vortex atoms. *Phil. Mag.* **34** (4), 15–24.

Thomson, W. 1880 Vibrations of a columnar vortex. *Phil. Mag.* **10** (5), 155–168.

Tritton, D. J. 1992 Stabilization and destabilization of turbulent shear flow in a rotating fluid. *J. Fluid Mech.* **241**, 503–523.

Verzicco, R., Jiménez, J. & Orlandi, P. 1995 On steady columnar vortices under local compression. *J. Fluid Mech.* **299**, 367–388.

Verzicco, R. & Orlandi, P. 1996 Wall/vortex-ring interactions. *Appl. Mech. Rev.* **49**, 447–460.

Verzicco, R., Orlandi, P., Eisenga, A. H. M., Heijst, G. J. F. van & Carnevale, G. F. 1996 Dynamics of a vortex ring in a rotating fluid. *J. Fluid Mech.* **317**, 215–239.